Simulations suggest robust microtubule attachment of kinesin and dynein in antagonistic pairs

Running title: Modeling bidirectional transport

Tzu-Chen Ma, Allison M. Gicking, Qingzhou Feng, and William O. Hancock*

Department of Biomedical Engineering, Pennsylvania State University, University Park, PA 16802

* Corresponding author: woh1@psu.edu

Abstract:

Intracellular transport is propelled by kinesin and cytoplasmic dynein motors that carry membrane-bound vesicles and organelles bidirectionally along microtubule tracks. Much is known about these motors at the molecular scale, but many questions remain regarding how kinesin and dynein cooperate and compete during bidirectional cargo transport at the cellular level. The goal of the present study was to use a stochastic stepping model constructed by using published load-dependent properties of kinesin-1 and dynein-dynactin-BicD2 (DDB) to identify specific motor properties that determine the speed, directionality, and transport dynamics of a cargo carried by one kinesin and one dynein motor. Model performance was evaluated by comparing simulations to recently published experiments of kinesin-DDB pairs connected by complementary oligonucleotide linkers. Plotting the instantaneous velocity distributions from kinesin-DDB experiments revealed a single peak centered around zero velocity. In contrast, velocity distributions from simulations displayed a central peak around 100 nm/s, along with two side peaks corresponding to the unloaded kinesin and DDB velocities. We hypothesized that frequent motor detachment events and relatively slow motor reattachment rates resulted in periods in which only one motor is attached. To investigate this hypothesis, we varied specific model parameters and compared the resulting instantaneous velocity distributions, and we confirmed this systematic investigation using a machine learning approach that minimized the residual sum of squares between the experimental and simulation velocity distributions. The experimental data were best recapitulated by a model in which the kinesin and dynein stall forces are matched, motor detachment rates are independent of load, and the kinesin-1 reattachment rate is 50 s^{-1}. These results provide new insights into motor dynamics during bidirectional transport and put forth hypotheses that can be tested by future experiments.

Statement of significance:

Bidirectional transport of vesicles along microtubules is vital for cellular function, particularly in the highly elongated axons and dendrites of neurons, and transport defects are linked to neurodegenerative diseases. For developing future therapeutic strategies, a better understanding is needed for how motors, cargo adapters, and accessory proteins coordinate their activities to transport cargo to their proper cellular locations. We approached this problem by simulating how antagonistic kinesin and dynein motors compete in pairs. We constrain our simulations by recent experimental results and conclude that the motors spend nearly all their time attached to the microtubule and competing against one another. This behavior is not predicted by existing single-molecule experiments and thus provides new insights into bidirectional transport.

Introduction:

Kinesin and dynein motor proteins carry out anterograde and retrograde transport in cells (1,2) and work together to achieve long-distance bidirectional transport in neurons (1,3-6). Coordinated transport is important for neuron growth and function (7-9), and dysfunction can lead to neurodegenerative diseases such as ALS and Alzheimer's (8,10,11). However, the mechanisms through which kinesin and dynein cooperate during cargo transport are unclear. Tracking of vesicles and other cargo in cells can reveal the complex dynamics of bidirectional transport (5,12-15), but this approach does not allow direct observation of the motors involved, and interpretations are complicated by the many regulatory factors that control intracellular transport (9). Single-particle tracking and optical tweezer studies have uncovered key details of the mechanisms by which individual motor proteins walk along microtubules (16-18), but apart from a few exceptions (19-23), experiments involving antagonistic motor pairs or teams are lacking. Computational simulations provide a valuable tool to bridge the gap between single-motor studies *in vitro* and cargo transport observations in cells, and these approaches help to uncover aspects of motor function that are difficult to observe through experiments.

A number of stochastic stepping models have been developed to simulate microtubule-based transport by kinesin and dynein motors (24-29). These models are parameterized based on single-particle tracking and optical tweezer experiments, and the simulation results can be used to investigate the influence of

specific motor parameters on the resulting bidirectional transport directionality and speed. However, one challenge is that bidirectional cargo trajectories are inherently complex and involve both directional switching and fluctuating velocities, making it difficult to quantitatively compare simulations and experiments. A second challenge is that simulation results are highly dependent on choices of specific parameters that describe motor stepping and motor-microtubule binding/unbinding kinetics, and in many cases these parameters are not tightly constrained by existing experiments.

There have been several experimental developments over the last few years that motivate the next generation of bidirectional stepping models. The first is the appreciation that traditional single-bead optical tweezers create non-negligible vertical forces normal to the microtubule that can accelerate the detachment of kinesin under load (30). This effect was clearly demonstrated by the finding that, compared to the single-bead assay, the kinesin-1 attachment duration at stall increases substantially in a three-bead assay, where vertical forces are eliminated (31). The second major development is the finding that cytoplasmic dynein activated by cargo adaptors such as BicD2, BicDR1, and Hook3 is highly processive and can generate forces in the range of kinesins (32-39). A third important discovery was that activated dynein complexes such as dynein-dynactin-BicD2 (DDB) frequently switch between three motility states – processive, paused, and diffusive – when engaged with a microtubule (34,37,40). Computational simulations provide an important tool to unravel how these different factors play into the bidirectional transport achieved by pairs or teams of kinesin and dynein motors.

The goal of present work is to incorporate recent kinesin and DDB experimental insights into a stochastic stepping model that recapitulates the bidirectional transport behavior of single kinesin-1 and DDB motor pairs. Parameter sensitivity tests and an objective machine learning approach explored the influence of motor detachment/reattachment dynamics and stall force parameters on the resulting bidirectional transport dynamics. The simulations were tuned to match recent in vitro experiments that tracked the dynamics of kinesin-DDB (Kin-DDB) pairs connected through complementary DNA hybridization. We found that incorporating detachment and reattachment rates inferred from published work resulted in directional switching and fast plus- and minus-end velocities not observed in the experiments. Instead, experimental data were best recapitulated by a model that incorporated matched stall forces and load insensitive detachment for both kinesin-1 and DDB. Thus, these simulations predict that motors working in antagonistic pairs have different properties than motors in isolation, and these properties enhance competition between kinesin and dynein.

Methods:

Stochastic stepping algorithm

Kin-DDB bidirectional transport was simulated using an updated and modified version of a previously published model (27) consisting of one kinesin and one dynein attached to a virtual cargo. At each timepoint, any attached motor can step forward by 8 nm, step backward by 8 nm, or detach from the microtubule; any detached motor can reattach to the microtubule. In the DDB switching model, an attached DDB motor can also switch between processive, diffusive, and stuck states. The decision for what event occurs and the time of the transition is decided by time evolution of the system using the Gillespie Stochastic Simulation Algorithm (41), as follows. For an event with a first-order transition rate constant, *k*, the transition time is generated as:

$$t = \frac{1}{k} \ln \frac{1}{R} \tag{1}$$

where R is a uniformly distributed random number in range 0 to 1. In a system with N possible events, the rate of any event occurring equals the sum of the rate constants for all possible events. Thus, at each time point, a two-stage process (the 'direct method' of Gillespie (41)) was used to determine the time and identity of the next transition. First, a random number R_1 is generated and used to compute the time to the next event, *i* as follows:

$$t = \frac{1}{\sum_{i=1}^{N} k_i} \ln \frac{1}{R_1} \tag{2}$$

In the second stage, a new round of random number generation is used to determine which of all possible events occurs; here, the probability of any event occurring is proportional to its rate constant (27,41). We split this stage into two steps, with the goal of modularizing the code and enabling expansion to multiple motors bound to the same cargo. We define *j* = 1,…M motors in the simulation (for our Kin-DDB simulations, M = 2). For each motor, *j*, there are *i* = 1,…N possible transitions, where N = 4 in most cases for our model (forward step, backward step, attachment and detachment). In the first step, a uniformly distributed random number, R_2 is generated and used to choose which of the M motors present will make a transition, and in the second step a random number R_3 is used to choose which of the N possible transitions for that motor will occur. Formally, using M motors, the probability of motor *j*, which has N possible transitions acting is:

$$P_j = \frac{\sum_{i=1}^{N} k_{ij}}{\sum_{j=1}^{M} \sum_{i=1}^{N} k_{ij}} \tag{3}$$

From N possible events on motor j, the probability of event i with rate constant k_{jj} occurring is:

$$P_i = \frac{k_i}{\sum_{i=1}^{N} k_i} \tag{4}$$

Where $\sum_{=1}^{N} P_i = \sum_{j=1}^{M} P_j = 1$. To identify the next event, the unit interval is divided into segments corresponding to each possible transition: $\left(0, \frac{k_1}{\sum k_i}\right], \left(\frac{k_1}{\sum k_i}, \frac{k_1+k_2}{\sum k_i}\right], \ldots, \left(\frac{\sum k_i - k_N}{\sum k_i}, 1\right]$. A random number is then used to determine which transition will occur. This method is repeated until all motors detach from the microtubule or a maximum run length or run duration is reached.

In the simulations, force is defined as positive in the plus-end direction and negative in the minus-end direction; thus, for kinesin-1 negative forces are hindering loads and positive forces are assisting loads. The force, *F*, applied to each motor is defined as the motor-cargo distance, Δx, multiplied by stiffness of the motor, κ_{motor}:

$$F = \kappa_{motor} * \Delta x \tag{5}$$

In our previous model (27), we used $\kappa_{kin} = 0.3$ pN/nm and $\kappa_{DDB} = 0.065$ pN/nm based on published work (42-44). For investigating the role of stiffness in the present work, we simplified the model by incorporating an identical stiffness, $\kappa_{motor} = 0.1068$ pN/nm for each motor, which sets the cargo at the midpoint between two motors.

At every timepoint, the position of the virtual cargo is set by computing a force balance between the two motors when both motors are attached, and by setting it to the position of the attached motor if only one motor is attached. Thus, following a motor step or detachment, the time for the system to reach mechanical equilibrium is assumed to be negligible. This instantaneous force balance can be justified by considering the relaxation time of the ~30 nm quantum dot attached to the Kin-DDB complex in the experiments. The drag coefficient γ_{Qdot} of a microsphere with radius r_{Qdot} = 15 nm in an aqueous solution (viscosity coefficient $\eta = 10^{-9}$ pN·s/nm^2) is given by the Stokes' law as $\gamma_{Qdot} = 6\pi\eta r_{Qdot} = 2.8 \times 10^{-7}$ pN·s/nm (45). Following a motor step, we can calculate the characteristic relaxation time constant for the particle to exponentially relax back to an equilibrium position as $\tau = \gamma_{Qdot}/\kappa_{motor}$, where $\kappa_{motor} = 0.1068$ pN/nm. This calculation yields a 3-microsecond relaxation time constant, which is negligible compared to the motor stepping and attachment/detachment rates in the msec range or slower.

Kinesin-1 simulation parameters

The kinesin-1 stepping model incorporates a linear force-velocity relationship with a constant backstepping rate, based on published optical tweezer measurements (46,47). The kinesin unloaded velocity, v^0 = 515 nm/s (Fig. S1A) was determined by carrying out single-molecule total internal reflection

142 fluorescence experiments in the buffer used for the published Kin-DDB experiments (30 mM HEPES, 1 mM
143 EGTA, 50 mM K-acetate, 2 mM Mg-acetate, 10% glycerol, 1 mM ATP, 10 µM Taxol, 0.2 mg/ml casein, pH
144 7.4) (34). The motor velocity is equal to the net stepping rate multiplied the 8 nm step size, $v =$
145 $\left(k_{forward} - k_{back}\right) * 8\,nm$. Under assisting loads, the motor velocity is constant and equal to the
146 unloaded velocity (46,47). Under hindering loads the velocity decreases linearly to zero at the stall force
147 (F_{stall} = 8 pN), where the forward and backwards stepping rates are equal, and plateaus at the constant
148 and load-independent backstepping rate, k_{back} of 3 s^{-1} (46,47). Based on the measured unloaded
149 velocity and the constant backstepping rate, the unloaded forward stepping rate, $k^0_{forward}$ is defined as:

$$k^0_{forward} = \frac{v^0}{8\,nm} + k_{back} \tag{6}$$

150 Under hindering loads up to the limit where $k_{forward}(F) = 0$, the load-dependent forward stepping rate
151 is:

$$k_{forward}(F) = \left(k_{back} - k^0_{forward}\right) * \left(\frac{|F|}{F_{stall}}\right) + k^0_{forward} \tag{7}$$

152 The kinesin-1 microtubule detachment rate $k_{detach}(F)$ varied exponentially with load (F):

$$k_{detach}(F) = k^0_{detach} * e^{\frac{|F|}{F_{detach}}} \tag{8}$$

153 Here, k^0_{detach} is the unloaded detachment rate, and the detachment force parameter $F_{detach} = \frac{k_B T}{\delta}$,
154 where k_B is Boltzmann constant, T is absolute temperature, and δ is a distance parameter that defines
155 the load-sensitivity of detachment. Based on Andreasson et al. (47), the unloaded detachment rate,
156 k^0_{detach} and the detachment force parameter, F_{detach} were set to 1.11 s^{-1} and 6.83 pN under hindering
157 loads, and 7.4 s^{-1} and 12.8 pN under assisting loads, respectively.

158 **DDB simulation parameters**

159 The DDB kinetic model is based on load-dependent velocity measurements by Elshenawy et al. (33), with
160 simplifications to enable more straightforward parameter sensitivity tests. The DDB step size in both
161 directions was set to 8 nm, the stall force was set to 3.6 pN, and a constant and load-independent
162 backstepping rate, k_{back} = 15 s^{-1} was included (33). The unloaded velocity of DDB was set to 328 nm/s
163 based on published control experiments carried out in parallel with the Kin-DDB experiments (34). Under
164 hindering loads (which are positive for DDB), a linear DDB force-velocity curve was used, similar to Eq. 7
165 for kinesin, up to the force at which $k_{forward}(F)$ reached zero. Under assisting loads (which are negative
166 for DDB and occur only in rare instances where DDB is positioned to the plus-end of kinesin-1), the load-
167 dependent DDB velocity was taken from published work (33):

$$v(F) = v_{min} * [1 - e^{(F_{stall}-F)*\frac{d}{k_B T}}] \quad (9)$$

168 Here v_{min} is the asymptotic velocity under super stall force, equal to -201 nm/s, and d is the characteristic
169 distance of 1.5 nm that defines the load-dependence of the stepping rate (33). In these assisting load
170 cases, the load-dependent forward stepping rate, $k_{forward}(F)$ was calculated as:

$$k_{forward}(F) = \frac{v(F)}{8\,nm} + k_{back} \quad (10)$$

171 The DDB detachment rate, k_{detach}, was modeled with an exponential load dependence similar to kinesin
172 (Eq. 8), with k^0_{detach} of 0.1 s^{-1} and F_{detach} of 3 pN, based on experimental work from Belyy et al. (32).

173 **DDB state-switching model**

174 In a subset of simulations, we incorporated DDB state switching based on work from Feng et al. showing
175 that DDB switches between processive, diffusive and stuck states during movement (34). To simulate this
176 behavior, three motility states for DDB were integrated into the model, as follows. In the processive state,
177 DDB can move forward, backward, or detach; in the stuck state, DDB cannot move or detach from the
178 microtubule; and in the diffusive state, DDB offers no resistance to kinesin movement and can also detach
179 from the microtubule. From every state, the motor can transition to either of the remaining states, with
180 transition rates as follows: the processive-to-stuck switching rate was 1.0 s^{-1} with reverse rate of 1.8 s^{-1};
181 the stuck-to-diffusive switching rate was 0.07 s^{-1} with a reverse rate of 0.33 s^{-1}; and the diffusive-to-
182 processive switching rate was 3.9 s^{-1} with a reverse rate of 0.23 s^{-1} (34). In the state-switching model
183 simulations, these transitions were added to the stepping and attachment/detachment transition
184 possibilities for DDB. For the majority of the simulations, this state switching was turned off.

185 **Data processing**

186 After running the simulations, the raw data were processed to match the experimental conditions (34),
187 as follows. To match the 20 fps frame rate (34), cargo position was averaged over 50 ms windows. To
188 account for uncertainties in fitting the experimental point spread function, a normally distributed error
189 with an 8 nm standard deviation was added to cargo position at each time point. The instantaneous
190 velocity at each timepoint was calculated by taking three-point slope of positions 50 ms before and after
191 each point.

192 **Parameter optimization**

193 As an alternate approach for parameter identification, we used a Bayesian Optimization method for
194 minimizing the residual sum of squares (RSS) between the experimental and model instantaneous velocity
195 distributions. The instantaneous velocity probability density functions from -2000 nm/s to 2000 nm/s with

10 nm/s bin widths were calculated for both experimental data and simulation results, where P_i is the PDF of instantaneous velocity *i*. For each parameter set, a velocity probability density function was generated from 1000 trajectories having a maximal run time of 50 s. The Matlab function 'bayesopt' was used with 100 iterations to identify parameter sets that minimized the RSS function:

$$RSS = \sum_i \left(P_i^{Exp} - P_i^{model}\right)^2 \tag{11}$$

201 **Results:**

202 **Formulation of bidirectional stepping model**

203 In recently published experiments, we reconstituted bidirectional cargo transport *in vitro* by connecting a
204 truncated kinesin motor to an activated dynein-dynactin-BicD2 (DDB) complex through complementary
205 single stranded DNA oligonucleotides (34). A quantum dot was then linked to a biotin on one end of the
206 DNA (Fig. 1A), and the position of the fluorescent cargo was tracked via total internal reflection
207 fluorescence (TIRF) microscopy at 20 frames per second. Consistent with previous work (33), the resulting
208 complexes moved slowly for long durations along immobilized microtubules, with some complexes
209 moving net plus-end and others moving net minus-end (Fig. 1C) (34). To better understand the kinesin
210 and dynein motor dynamics underlying this bidirectional transport, we adapted a previously published
211 Kin-DDB transport bidirectional transport model, carried out simulations, and compared predictions from
212 the simulations to the new experimental data. The model uses the Gillespie Stochastic Simulation
213 Algorithm (41), as described in Methods and our previous publication (27). At every time point, either
214 motor can step forward, step backward, detach from or reattach to the microtubule, with the probability
215 of each transition being proportional to its first-order rate constant (Fig. 1B; diagram of the algorithm is
216 given in Fig. S2). The simulated cargo has neither mass or drag, and its position is updated following every
217 step to maintain force balance. The parameters for this 'basic model' are shown in Table 1.

Parameter	Basic model		Best-fit model		Reference
	Kinesin-1	DDB	Kinesin-1	DDB	
Unloaded velocity (nm/s)	515	328	515	328	(34), Fig. S1A
Backstepping rate (s^{-1})	3	15	3	1	(33,46)
Stall force (pN)	8	3.6	6	6	(29,33,46)
Unloaded detachment rate (s^{-1})[a]	1.11	0.1	1.11	0.1	(32,37,40,47)
Detachment force (pN)[a]	6.8	3	Ideal	Ideal	(32,37,40,47)
Reattachment rate (s^{-1})	5	5	50	5	(48)
Stiffness (pN/nm)	0.1068	0.1068	0.2	0.2	(42-44)

218 *Table 1. Parameters used for the initial 'basic' model and the final 'best-fit' model. Parameters for the 'better-fit' model are given*
219 *in Table S1.*
220 [a] *For kinesin under assisting loads, the unloaded detachment rate extrapolation was 7.4 s^{-1} and detachment force was 12.8 pN*
221 *based on (47). For DDB under assisting loads, the unloaded detachment rate and detachment force were identical to the hindering*
222 *load condition. Ideal bond (load-independent detachment) corresponds to F_{detach} equal to infinity.*
223

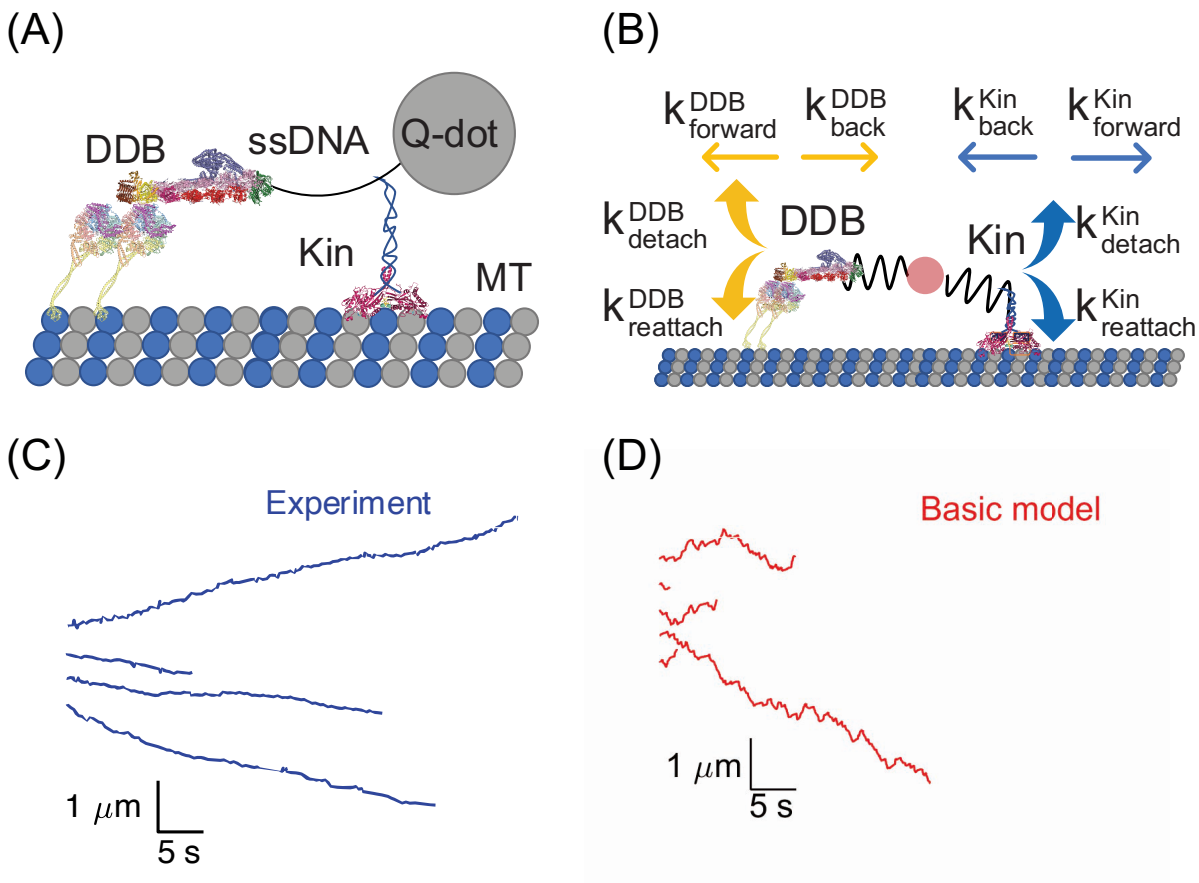

Figure 1. (A) Schematic of Kin-DDB bidirectional transport tracking experiment in which motors are connected together by a complementary single stranded DNA (ssDNA) and attached to a quantum dot for visualization by fluorescence microscopy (34). (B) Stochastic model of Kin-DDB bidirectional transport showing the different rate constants incorporated into the simulations. (C) Example individual distance versus time traces of experimental data from published work by Feng et al (34). (D) Simulation traces from the basic model. Kinesin and DDB images adapted from PDB files 6A1Z and 3VKH (49-51).

231 **Comparing bidirectional stepping simulations to experimental data**

232 We next simulated bidirectional stepping of a complex containing one kinesin-1 and one DDB motor to
233 determine the degree to which the simulations can recapitulate the experimental results (Fig. 1C). The
234 mean velocities of trajectories from the simulations (-4.4 ± 115 nm/s mean and standard deviation; N =
235 1000) were similar to the experimental velocities (-8.2 ± 47 nm/s mean and standard deviation; N = 30).
236 However, the simulated trajectories contain fluctuations and directional switching not seen in the
237 experiments (Fig. 1C and D). One explanation for the larger fluctuations in the simulated traces is that
238 experimental temporal and spatial resolution limits are obscuring fluctuations in the experimental data.
239 Therefore, to enable more accurate comparison between experiments and simulations, we added
240 simulated experimental noise and reduced the temporal resolution to the simulations, as follows. From
241 the quantum dot tracking experiments (34), we determined the experimental error in the Gaussian fits to
242 the point-spread function data to be 8 nm; thus we added a normally distributed noise term with a
243 standard deviation of 8-nm to each point in the simulation. Second, we binned the simulated data to 50
244 ms to match the 20 per second frame rate of the experiments.

245 To better compare the fluctuations in the traces resulting from motor stepping dynamics, we examined
246 5-second segments of experimental and simulated traces. Despite the downsampling, larger and more
247 frequent fluctuations can be seen by eye in the simulated traces compared to the experimental traces (Fig.
248 2A and B). A Mean Square Displacement (MSD) analysis quantitatively confirmed this: simulated traces
249 had an apparent diffusion coefficient of 11,800 nm^2/s, compared to 996 nm^2/s for the experiments (Fig.
250 S1B). To better compare the experimental and simulated velocities, we calculated the instantaneous
251 velocities over 100-ms time windows for both the experimental and simulation results and plotted the
252 instantaneous velocity distributions (Fig. 2C). The experimental instantaneous velocity distribution had a
253 prominent single peak centered at -12 nm/s, and 95% of the distribution was between -394 and 371 nm/s.
254 In contrast, the simulated instantaneous velocity distribution had a distinct central peak that was right
255 shifted compared to the experiments, along with distinct side peaks corresponding to the unloaded
256 velocities of DDB and kinesin-1. Using a Gaussian mixture model (GMM), the velocity distribution was fit
257 well by three normal distributions: a peak centered at 127 nm/s that accounted for 53% of the population,
258 a minor peak at -334 nm/s that accounted for 41% of the population, and another minor peak centered
259 at 587 nm/s that accounted for 6% of the population (Table 2). The motor reattachment rate in our
260 simulations was 5 s^{-1} based on published experimental data for kinesin-1 (48,52,53), and because
261 equivalent experimental data are not available for dynein, we chose the same value for the DDB complex

262 (Table 1). This relatively slow reattachment rate means that when either motor detaches from the
263 microtubule, it will take on average 200 ms to reattach, giving the other motor time to move at its
264 unloaded velocity. Thus, these lateral peaks in the simulated velocity distribution can be explained by the
265 simulations having more periods when only one motor is attached than the experiments, and their
266 positions are close to the unloaded kinesin and DDB velocities.

	Experiments	**Basic model**	**Best-fit model**
Central peak	-18 nm/s (65%)	127 nm/s (53%)	-8 nm/s (93%)
Plus-end peak	98 nm/s (23%)	587 nm/s (6%)	452 nm/s (0.5%)
Minus-end peak	-204 nm/s (11%)	-334 nm/s (41%)	-319 nm/s (6.5%)
Residual sum of squares (RSS)		$3.93*10^{-5}$	$2.76*10^{-6}$

267 *Table 2. Gaussian Mixture Model fits to instantaneous velocity distributions. Experimental data from Feng et al. (34) include N =*
268 *30 traces and basic and best-fit models both include N = 1000 traces. Percentages are the relative integrated weights of each*
269 *mode. Fits used the "fitgmdist" function in MATLAB with three Gaussians having initial values of 0, 500, and -300 nm/s). RSS values*
270 *denote the residual sum of squares between the probability density functions each model and the experimental data.*

271 To better understand the underlying motor dynamics that lead to the experimental Kin-DDB traces being
272 relatively smooth and the velocity distribution having a single peak centered around zero, we investigated
273 how the modeled properties of kinesin-1 and DDB contribute to the distinctive instantaneous velocity
274 distribution of our 'basic' model described above. We hypothesize that there are properties of kinesin-1
275 and/or DDB motors that differ when the motors are joined in a two-motor complex compared to in their
276 isolated states in the single-molecule fluorescence and optical trapping experiments used to develop the
277 basic model. To test this overarching hypothesis, we varied motor parameters and quantified the change
278 in performance, with the goal of reducing the magnitude of the fast plus- and minus-end velocity peaks
279 in the instantaneous velocity histogram (Fig. 2C) to better match the experimental results.

280

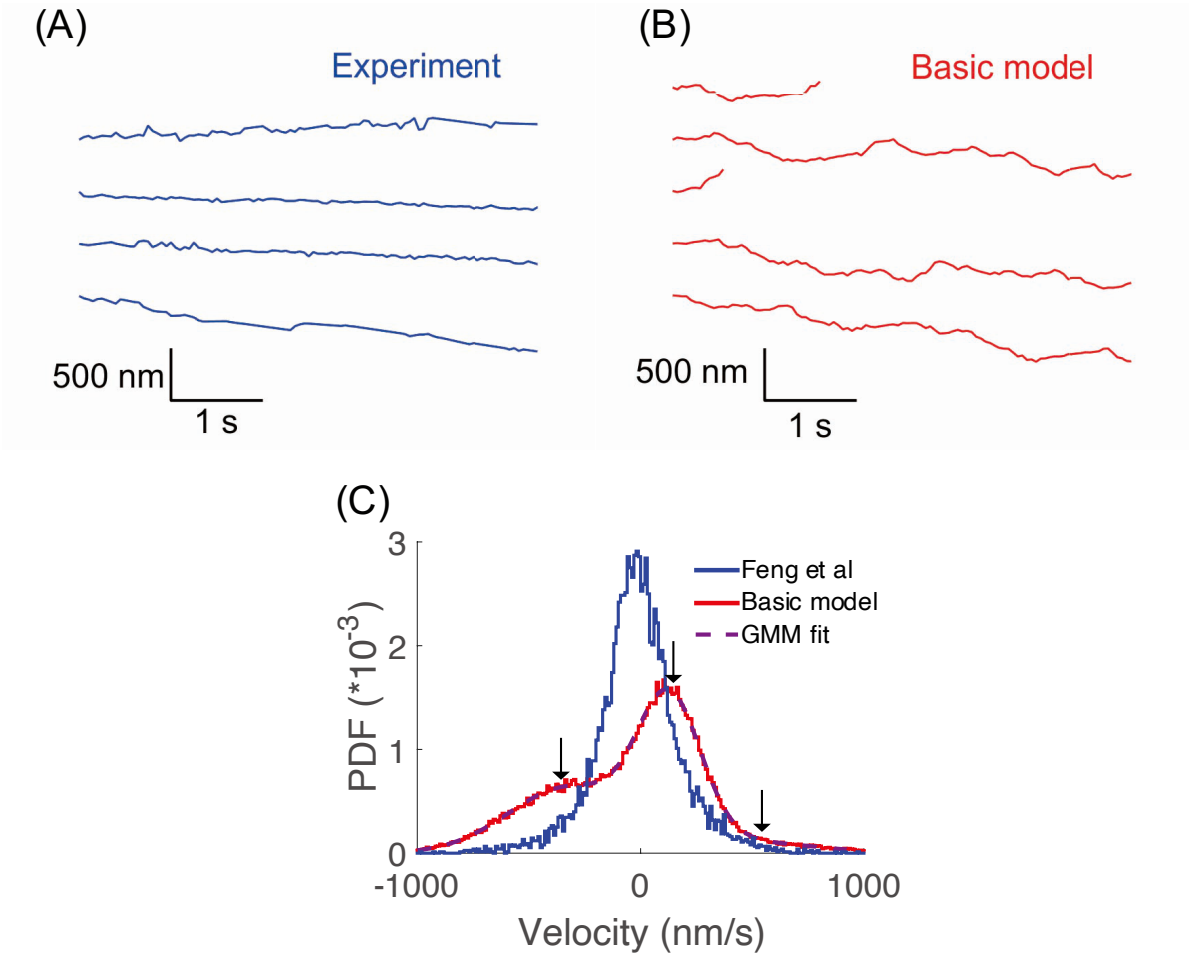

Figure 2. Comparison between simulation results and experimental data from Feng et al. (34). (A and B) Example individual distance versus time traces over a 5-second window, showing that simulation traces contain more fluctuations than the experimental traces. Model traces were downsampled to 20 Hz and positional noise was added to more accurately match experimental conditions. (C) Instantaneous velocity distribution (averaged over 100 ms windows with 10 nm/s bin width), showing three peaks in the simulation results (red, N = 1000 traces), but only a single central peak in the experimental distribution (blue, N = 30 traces). Parameters for Gaussian mixture model (GMM) fit are given in Table 1.

290 **Testing the influence of dynein motor properties on bidirectional transport**

291 The first hypothesis we tested was that the simulations differ from the experiments because the motile
292 properties of DDB in a bidirectionally moving Kin-DDB complex differ from the DDB properties measured
293 in single-motor optical tweezer experiments. To test this possibility, we first investigated whether either
294 including experimentally observed pausing and diffusive states of the DDB complex could better align the
295 simulations with the experiments. In virtually all published unloaded single-molecule studies, DDB exhibits
296 long processive runs, but also undergoes episodes of 1D diffusion along the microtubule and spends a
297 significant fraction of the time stuck to the microtubule in an immobilized state (32,34,37,38). Feng et al
298 found that DDB spent 65% of the time in a processive state, 31% of the time in a stuck state, and 4% of
299 the time in a diffusive state, and also quantified the switching rates between states (34). We incorporated
300 this DDB switching behavior as a series of transitions into our model. We assumed that the diffusive state
301 of DDB offered no resistance to kinesin stepping, and that in the stuck state, DDB neither moved nor
302 detached from microtubule. In the instantaneous velocity distribution, incorporating this DDB switching
303 behavior caused a decrease in the magnitude of the unloaded DDB velocity peak, but had no effect on the
304 unloaded kinesin velocity peak (Fig. 3A). The fall in the unloaded DDB peak can be explained by DDB
305 spending time in the stuck state instead of processive walking. The lack of change in the unloaded kinesin
306 peak is likely due to the fact that DDB is in the diffusive state only a small fraction of the time (Fig. 3A).
307 Thus, DDB state switching cannot account for the discrepancy between model and experimental results.
308 Due to this lack of an effect, all subsequent simulations used only a single processive state for DDB.

309 The second property we examined was the load-dependent detachment dynamics of DDB. There is
310 abundant evidence in the literature that dynein alone has catch-bond behavior, meaning that the
311 detachment rate slows down with increasing load (26,29,54-57). There is no experimental evidence to our
312 knowledge that activated dynein in a DDB complex shows catch-bond behavior; however, only one
313 published study directly addresses this question (33). Thus, we investigated whether the simulated
314 bidirectional behavior is shaped by the load-dependent detachment kinetics of DDB by using an
315 exponential dependence of the off-rate on load (Methods, Equation 8). In this formulation, a positive
316 detachment force parameter (F_{detach}) corresponds to a slip-bond, a negative value corresponds to a
317 catch-bond, and a value of infinity corresponds to an ideal-bond. We found that slowing the unloaded
318 detachment rate (k^0_{detach}) or increasing the detachment force (F_{detach}) decreased the peak
319 corresponding to the unloaded kinesin-1 velocity, bringing the distribution more in line with the
320 experimental (Fig. 3B and C). When an ideal bond was simulated by setting F_{detach} to infinity, the

321 instantaneous velocity distribution was indistinguishable to that for F_{detach} = 15 pN (Fig. S3A). Setting
322 F_{detach} to -3 pN, corresponding to a catch-bond resulted in no change from the ideal-bond model (Fig.
323 S3A).

324 The third property we examined was the DDB stall force, F_{stall}. In the literature, stall forces for isolated
325 dynein were measured to be 1 pN by a number of labs (29), but activated dynein in a DDB complex was
326 later shown to have a stall force of 3.6 pN (33). In our basic model, the kinesin stall force is twice that of
327 DDB (Table 1) and the central peak in the instantaneous velocity distribution is shifted towards the plus-
328 end by nearly 150 nm/s relative to the experimental peak (Table 2; Fig. 2C); thus, it is reasonable to expect
329 that bringing the stall forces more into alignment should shift the central peak. We found this to be the
330 case (Fig. 3D) – increasing the DDB stall force to 6 pN shifted the central peak leftward and increasing it
331 to 8 pN to match the kinesin stall force brought the central peak nearly into alignment with the
332 experimental peak. As a final investigation, we examined the sensitivity of the simulations to the DDB
333 reattachment rate by increasing k_{attach} from 5 s^{-1} to 50 s^{-1}. This modification had virtually no effect on
334 the simulated velocity distribution (Fig. S3B). This lack of an effect likely stems from the slow DDB
335 unloaded detachment rate of 0.1 s^{-1} – because DDB detachments are relatively infrequent, the unbound
336 episodes are rare and shortening their duration has little effect.

337 To summarize the DDB parameter investigations, removing the load-dependence of DDB detachment by
338 modeling DDB as an ideal-bond nearly eliminated the kinesin peak in the instantaneous velocity
339 distribution, and increasing the DDB stall force shifted the central velocity peak leftward, closer to the
340 experimental peak. In contrast, incorporating a switching model for DDB or increasing the DDB
341 reattachment rate had only minimal effects on the velocity distribution. Next, to explore other
342 modifications of the model that could diminish the DDB velocity peak, we examined the sensitivity of the
343 model simulations to changes in the kinesin detachment and reattachment rates.

344

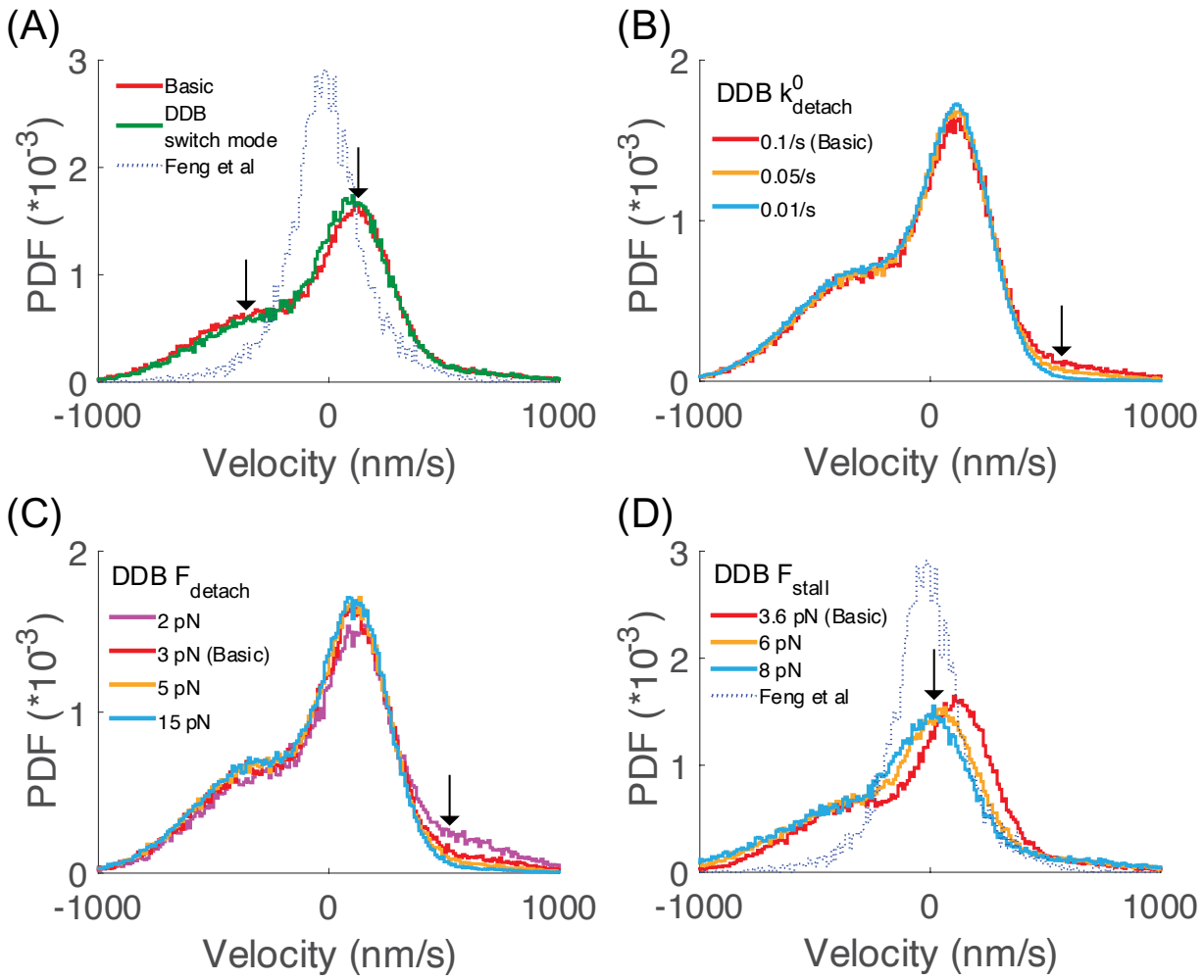

Figure 3. Effect of changing DDB parameters on the instantaneous velocity distribution. (A) Effect of incorporating switching between processive, diffusive and stuck states for DDB. Arrows denote the small changes in the central velocity peak and the minus-end side peak. (B) Effect of changing the DDB unloaded detachment rate, with arrow highlighting the resulting changes in the plus-end side peak. (C) Effect of changing the DDB detachment force, where larger F_{detach} denotes less load-sensitivity of detachment. (D) Effect of increasing the DDB stall force, with arrow denoting leftward shift of the central peak with increasing stall force.

354 **Testing the influence of kinesin-1 motor properties on bidirectional transport**

355 The second hypothesis we tested was that the discrepancy between simulations and experiments is due
356 to differences in the motor properties of kinesin when operating in an antagonistic motor pair compared
357 to single-bead optical tweezer experiments with isolated kinesin motors. These differences could be due
358 to, for instance, the different geometries of being attached to a trapped bead versus being tightly
359 connected to dynein through a short DNA (31,58,59), and they could in principle affect both motor on-
360 and off-rates. The first investigation was to determine whether decreasing the detachment rate of kinesin
361 by reducing k^0_{detach} or increasing F_{detach} reduced the magnitude of the DDB velocity peak in the
362 instantaneous velocity distribution. Decreasing k^0_{detach} for kinesin-1 substantially decreased the
363 magnitude of the unloaded DDB velocity peak and increased the magnitude of the central peak, although
364 it also increased the unloaded kinesin velocity peak (Fig. 4A). Increasing F_{detach} to reduce the sensitivity
365 of detachment to load had a similar effect but to a lesser degree (Fig. 4B), with the effect plateauing
366 around an F_{detach} value of 35 pN. Thus, decreasing the kinesin detachment rate diminished the minus-
367 end velocity peak, bringing the simulations closer to the experimental results, but neither of these changes
368 had a significant effect on the unloaded kinesin peak.

369 The other way to decrease the fraction of the time Kin-DDB complexes are moving solely by DDB is to
370 increase the kinesin-1 reattachment rate. In the 'basic' model, we set a constant reattachment rate,
371 $k_{reattach}$, of 5 s^{-1} for both motors, based on the literature (28,53). To determine whether the kinesin-1
372 reattachment rates were contributing to the simulation-experiment mismatch, we tested several larger
373 values of $k_{reattach}$ for each motor. In contrast to DDB where altering the reattachment rate had little
374 effect (Fig. 3D), increasing $k_{reattach}$ for kinesin-1 both strongly diminished the fraction of time the
375 complex moves at the unloaded DDB speed and increased the fraction of time that both motors are
376 engaged, resulting in an enhanced cargo velocity peak near zero (Fig. 4C).

377 The final kinesin parameter we investigated was the kinesin stall force, F_{stall}. In our 'basic' model, the
378 kinesin-1 stall force was set to 8 pN and the DDB stall force was set to 3.8 pN based on published optical
379 tweezer experiments (33,46,47). Because of this discrepancy, it is perhaps not surprising that when both
380 motors are engaged, the kinesin directionality dominates. Thus, we investigated kinesin stall forces
381 between 4 and 8 pN, which are in the range of published studies (29,46,60-64), and found that weaker
382 kinesin stall forces cause the central velocity peak to shift closer to zero, better matching the experiments
383 (Fig. 4D).

In summary, a major discrepancy between the experimental and simulated velocity distributions is the peak in the simulations near the unloaded DDB velocity. We found that this minus-end velocity peak could be diminished by decreasing the kinesin-1 unloaded detachment rate or the sensitivity of detachment to load, or by increasing the kinesin-1 reattachment rate. Additionally, decreasing the kinesin-1 stall force resulted in a leftward shift of the dominant peak in the velocity distribution, bringing the simulations in better alignment with experiments.

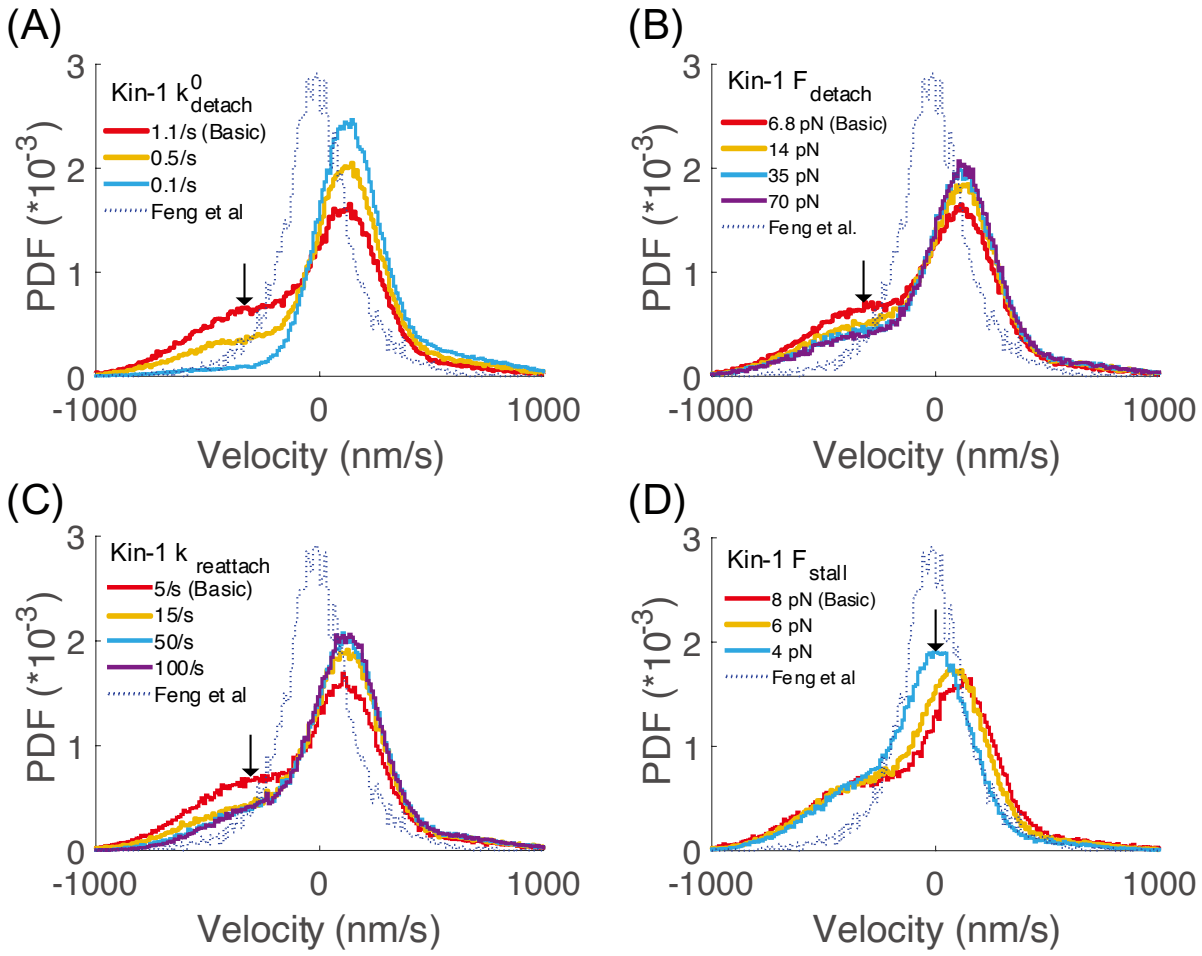

Figure 4. Effect of changing kinesin-1 parameters on the instantaneous velocity distribution. (A) Effect of decreasing the unloaded kinesin-1 detachment rate was to diminish the minus-end velocity peak and increase the central peak. (B) Effect of increasing the kinesin-1 detachment force parameter was to moderately diminish the minus-end velocity peak. (C) Effect of increasing the kinesin-1 reattachment rate was to diminish the minus-end velocity peak. (D) Effect of decreasing the kinesin-1 stall force was to shift the central velocity peak leftward to better match the experimental data.

398 **Tuning parameters in an improved bidirectional transport model**

399 The simulation results to this point showed that altering motor attachment and detachment rates can
400 decrease the weight of the instantaneous velocity distribution corresponding to the two unloaded motor
401 velocities, and that bringing the kinesin and DDB stall forces into closer alignment can shift the location of
402 the central peak. Informed by these single parameter adjustments, we next formulated an updated model
403 that incorporated multiple parameter adjustments, with the goal of more closely matching the simulated
404 and experimental instantaneous velocity distributions. We chose not to modify the k_{detach}^{0} parameter for
405 either kinesin-1 or DDB because single-molecule TIRF measurements from many labs have consistently
406 measured unloaded detachment rates (equal to velocity divided by run length) near 1 s^{-1} for kinesin-1 and
407 0.1 s^{-1} for DDB (29,40,46,47). Our adjustments to kinesin-1 were guided by recent work by Pyrpassopoulos
408 et al. (58), who showed that kinesin-1 KIF5B under purely horizontal loads, achieved through a three-bead
409 optical tweezer geometry, has a ~6 pN stall force, a 1.1 s engaged duration (matching the unloaded run
410 duration) (58), and a component of its reattachment rate at 100 s^{-1} (31,58). Thus, we set the kinesin-1 stall
411 force to 6 pN and applied an ideal-bond detachment model by setting $k_{detach}(F) = k_{detach}^{0}$. We also
412 increased the kinesin-1 reattachment rate to 50 s^{-1}; a 100 rate s^{-1} was not used because there was little
413 improvement beyond 50 s^{-1} and because in the experiments there were components slower than 100 s^{-1}
414 (58). There is no comparable three-bead study for DDB, but we hypothesize that removing the vertical
415 force component may have similar effects on dynein. Thus, we also incorporated a load-independent
416 detachment rate (ideal bond) for DDB.

417 The parameter adjustments were incorporated into an upgraded model that we named the 'better-fit'
418 model (Table S2). Simulations showed that in the 'better-fit' model the plus-end side peak was eliminated,
419 the minus-end side peak was diminished, and the central peak was substantially enhanced but was still
420 right-shifted compared to the experimental data (Fig. 5A). Starting from this improved model, we tested
421 further parameter adjustments, with the goal of shifting the central velocity peak to the left and
422 eliminating the minus-end side peak. We first tested the DDB stall force and found that increasing it to 6
423 pN to match that of kinesin-1 substantially shifted the main peak leftward. Next, we varied the DDB
424 backward stepping rate and found that decreasing it to 3 s^{-1} or 1 s^{-1} also substantially shifted the main
425 peak leftward (Fig. 5C and S3C).

426 The final property we tested was the motor stiffness, which affects how rapidly motors ramp up their
427 force as they step in opposite directions. We found that increasing motor stiffness eliminated the fastest
428 minus-end velocities in the distribution, and that this weight was shifted to the central peak, bringing it

429 closer to the height of the experimental peak (Fig. 5D and S3D). Upon closer examination, we surmised
430 that this shift results from eliminating a 'recoil effect' occurring at lower stiffness values, in which the
431 kinesin detaches and the cargo rapidly moves toward the minus-end to become centered on the engaged
432 DDB motor. A 6 pN force is expected to stretch the spring that connects each motor to its cargo by 60 nm.
433 A recoil of this magnitude over the 0.1 s window used for the velocity distributions corresponds to a -600
434 nm/s velocity, and this is the component that is eliminated when motor stiffness is increased (Fig. 5D). In
435 summary, in the 'better-fit' model either increasing the DDB stall force or decreasing the DDB
436 backstepping rate shifted the central velocity peak leftward to better align with the experimental
437 distribution, and increasing the motor stiffness eliminated the remaining minus-end velocity side peak.

438

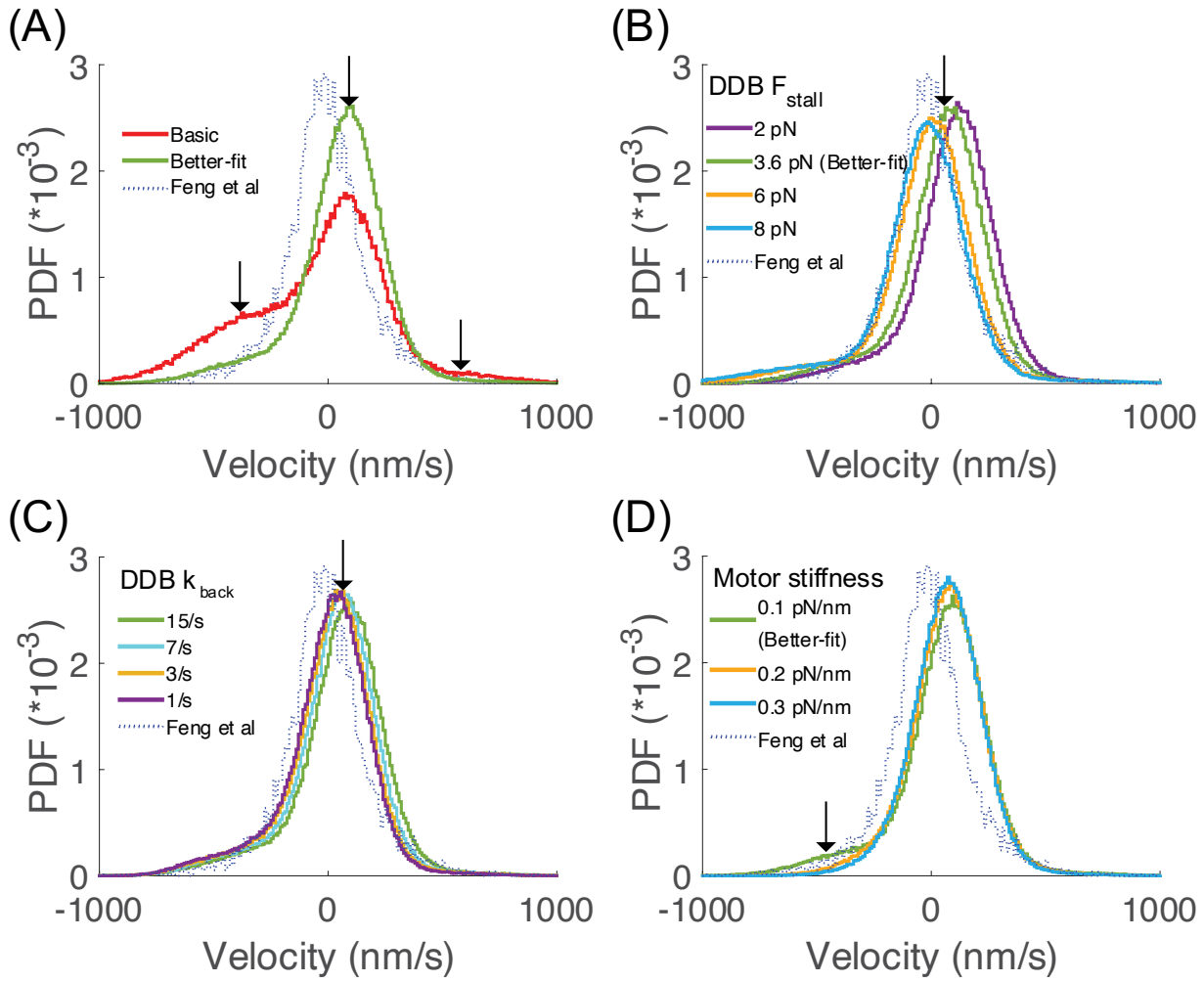

Figure 5. Results from 'better-fit' model. (A) Comparison between 'basic' and 'better-fit' models. The 'better-fit' model includes load-independent detachment kinetic for both motors, a 6 pN stall force for both motors, and a 50 s^{-1} reattachment rate for kinesin. Arrows denote the three velocity peaks that are altered. (B) Effect of altering the DDB stall force showed the leftward shift for larger stall forces. (C) Effect of decreasing the DDB backstepping rate is to shift the central velocity peak leftward. (D) Effect of increasing the motor stiffness was to eliminate the small minus-end velocity side peak that results from a motor 'recoil' effect at lower stiffness values.

448 **Using machine learning for parameter sensitivity exploration and optimization**

449 Having narrowed the parameter choices by iterative tuning, we next applied an automated parameter
450 optimization method to identify parameter sets that best match the simulations to the experimental
451 velocity distributions. To do this we used the Matlab Bayesian Optimization function 'bayesopt', which
452 identifies an optimal parameter set based on an objective function. We defined the objective function as
453 the residual sum of squares (RSS) between the experimental and simulation velocity distributions, and we
454 defined upper and lower search bounds for each parameter (Table 3). In the first round, we allowed seven
455 parameters to be optimized: the detachment forces and reattachment rates for both motors, along with
456 the motor stiffness, DDB stall force and DDB backstepping rate. Because of the interdependency of the
457 parameters, we found that repeated optimization runs achieved similar RSS values using different
458 parameter sets. Hence, in Table 3 we report the range of optimal parameter values for 10 independent
459 optimization runs, with large ranges connoting parameters that either co-vary with other parameters or
460 do not strongly affect the final velocity distribution, and narrow ranges connoting parameters that most
461 strongly determine model performance. As a final step, we fixed the detachment forces and reattachment
462 rates and performed a second round of optimization on the remaining DDB stall force, DDB backstepping
463 rate, and motor stiffness parameters. The results of this final optimization were similar to the first, but
464 the optimal ranges were narrowed (Table 3).

465 The parameter optimization results can be summarized as follows. First, the optimal detachment forces
466 for both motors were relatively high, consistent with the ideal-bond model we implemented in our
467 'better-fit' model. Therefore, in our final 'best-fit' model, we set detachment to be independent of load
468 for both motors. Second, consistent with the 'better-fit' model, the kinesin reattachment rate converged
469 in a range around 50 s^{-1} for kinesin and around 5 s^{-1} or slower for DDB. Thus, we chose those values for
470 the reattachment rates. Third, the DDB stall force converged near the 6 pN stall force of kinesin-1,
471 supporting the observation in Fig. 5B that matching the stall forces helps to align the central velocity peak
472 with the experiments. Fourth, the DDB backstepping rate converged in a range of 1-5 s^{-1}. This rate is slower
473 than the experimental 15 s^{-1} (33), and reiterates the finding in Fig. 5C that slowing DDB backstepping shifts
474 the central velocity peak leftward. Based on the optimal fit with the reduced parameter set, we set the
475 DDB backstepping rate to 1 s^{-1} (see Discussion). Finally, the motor stiffness converged at 0.2 pN/nm,
476 consistent with our finding that a minimum stiffnesses in this range is needed to avoid the 'recoil'
477 phenomenon that contributes unwanted minus-end velocities. The final parameter choices that were

used for the 'best-fit' model are shown in Table 3, and the entire 'best-fit' parameter set is provided in Table 1.

Parameter	Limits	Optimized parameter values		Final value
		7 parameter fit	3 parameter fit	
Kinesin-1 detachment force	0.01 - 50 pN	17 - 49 pN	Ideal bond	Ideal bond
DDB detachment force	0.01 - 50 pN	5 - 49 pN	Ideal bond	Ideal bond
Kinesin-1 reattachment rate	0.01 - 100 s^{-1}	30 - 96 s^{-1}	50 s^{-1}	50 s^{-1}
DDB reattachment rate	0.01 - 100 s^{-1}	0.3 - 86 s^{-1}	5 s^{-1}	5 s^{-1}
DDB stall force	0.01 - 6 pN	5.7 - 6 pN	5.9 - 6 pN	6 pN
DDB backstepping rate	1 - 20 s^{-1}	1 - 6 s^{-1}	1 - 4 s^{-1}	1 s^{-1}
Motor stiffness	0.01 - 0.3 pN/nm	0.2 - 0.3 pN/nm	0.18 - 0.22 pN/nm	0.2 pN/nm

Table 3. Motor parameters estimated by Matlab 'bayesopt' parameter optimization function using the limits shown for each parameter. Parameter ranges from 10 independent optimization runs are shown. From the seven parameter fit, four parameters were fixed at the values shown, and the three remaining parameters were then optimized. Final values refer to parameter values chosen for the 'best-fit' model.

Having identified a final parameter set, we characterized the resulting traces and quantified the fit to the experimental data. The displacement versus time traces for the 'best-fit' model were smoother by eye than the 'basic' model (Fig. 6A; compare to Fig. 2B, and Fig. S4A; compare to Fig. 1D), and similar to the experimental data (Fig. 2A). Using a mean squared displacement analysis, the apparent diffusion coefficient dropped from 11,800 nm^2s^{-1} in the 'basic' model to 1272 nm^2s^{-1} in 'best-fit' model, which was close to the 996 nm^2s^{-1} for the experimental data (Fig. S1B). More importantly, in the instantaneous velocity distribution (Fig. 6B), the unloaded velocity peaks, which were a significant discrepancy in the 'basic' model, were nearly eliminated, and the central peak was shifted to near zero to match the experimental data. One metric of this agreement is that in the 'best-fit' model, 95% of instantaneous velocity values fall between -349 to +299 nm/s, similar to the -394 to +371 nm/s range for the experimental data. Fitting the 'best-fit' velocity distribution to a Gaussian mixture model identified a central peak centered at -8 nm/s and comprising 93% of weight, along with two side peaks centered at 452 nm/s and -318 nm/s, comprising 0.5% and 6.5% of the weight, respectively (Table 2). Finally, the residual sum of squares (RSS) between experimental and simulation data dropped from $3.93*10^{-5}$ in the

'basic' model to $2.76*10^{-6}$ in 'best-fit' model (Table 2). Other features were also improved; for instance, the simulated traces for the 'best fit' model also had longer durations, more closely matching experiments (Fig. S4). Also, for the 'best-fit' model the distribution of velocities computed over each trace matched the experimental values (Fig. 6C).

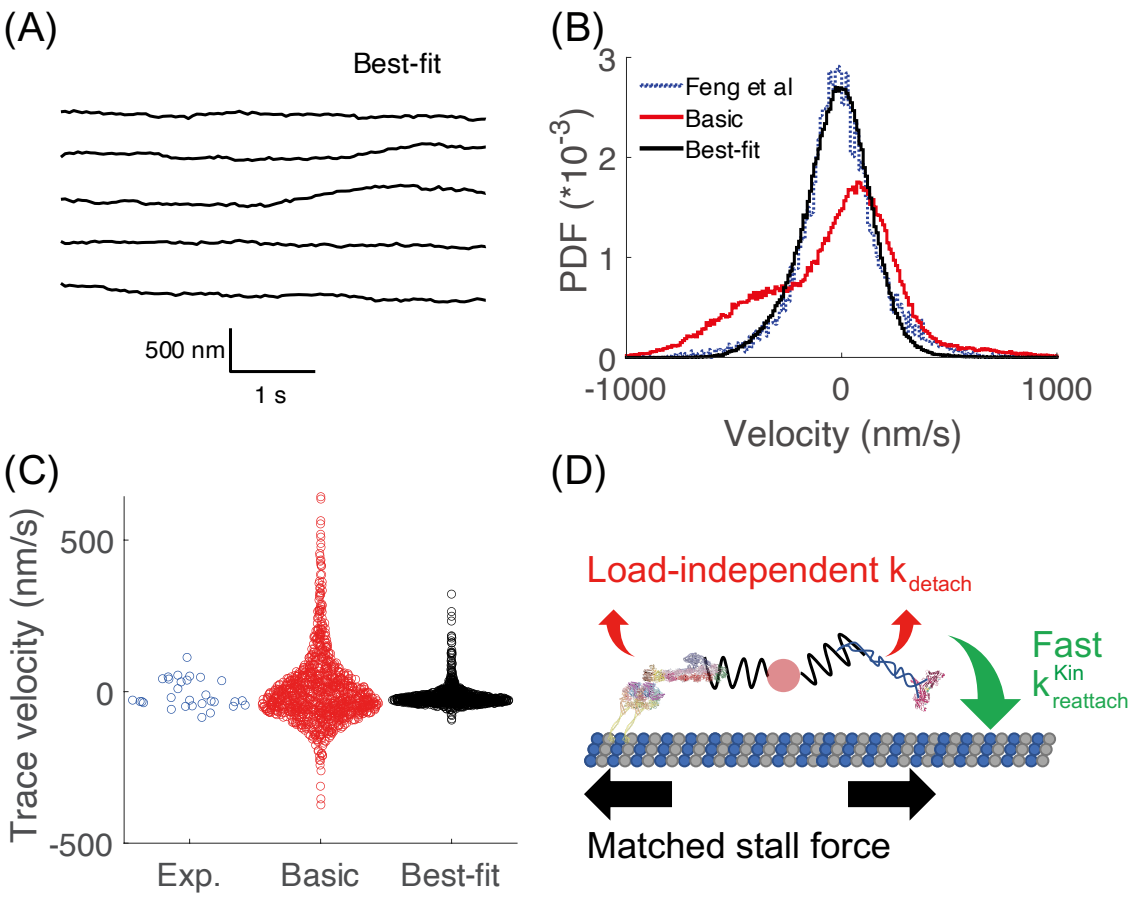

Figure 6. Results from 'best-fit' model. (A) Example traces from best-fit model. (B) Comparison of instantaneous velocity distributions between experimental data (blue), basic model (red) and best-fit model (black). (C) Comparison of trace velocity distributions for experimental data (blue), basic model (red), and best-fit model (black). (D) Diagram of the best-fit model for Kin-DDB bidirectional transport, highlighting parameter choices that resulted in optimal alignment with experimental data. The detachment rates of DDB and kinesin are independent of load (ideal-bond), and kinesin-1 reattaches to microtubule with a fast rate ($50\ s^{-1}$). These features maximize the fraction of time both motors are engaged and pulling against one another. Matching the kinesin and DDB stall forces (not shown) shifted the central velocity peak close to zero to match the experimental data.

515 **Discussion:**

516 Transport of vesicles in axons and dendrites involves varying numbers and types of motors, as well as
517 regulation at multiple levels. Hence, to understand how kinesin and dynein motors attached to the same
518 cargo compete and coordinate during transport, the field has turned to reconstituting the *in vitro* motility
519 of pairs of kinesin and activated dynein (1,7,38,53,65). This approach allows an examination of how
520 differing mechanochemical properties of specific motor isotypes translate into effective movement
521 against an antagonistic partner. Consistent behavior of kinesin-dynein pairs that are observed across
522 different labs (20,32-34) include the following: 1) Kin-DDB complexes remain bound to microtubules for
523 ~tens of seconds (33,34), considerably longer than kinesin-1 or DDB alone; 2) trajectories include episodes,
524 lasting from seconds to tens of seconds, where the velocity of the complex is ~10-fold slower than the
525 unloaded velocities of the respective motors; and 3) cargo trajectories are quite smooth and show few if
526 any directional switches. In principle, it should be possible to recapitulate these motility behaviors using
527 Kin-DDB simulations that incorporate established parameters for kinesin and dynein behavior in isolation.
528 However, we find this not to be the case. Instead, simulations of Kin-DDB transport in our 'basic' model
529 show frequent directional switches and significant proportions of time when the complexes move at the
530 unloaded velocity of the motors (Fig. 2B). The discrepancies between the simulations and experiments
531 were clearly seen by comparing the instantaneous velocity distributions (Fig. 2C). The experimental data
532 were centered in a wide peak around zero velocity, whereas the simulated data had additional peaks
533 corresponding to the unloaded kinesin-1 and DDB velocities, along with a central peak centered around a
534 slow plus-end speed. Thus, we focused our in silico 'experiments' on identifying parameter adjustments
535 that reconciled the simulations with the experiments.

536 The first modification that helped to align the simulation results with the experiments was to make the
537 kinesin detachment rate independent of load in the range of the stall forces used. Although single-bead
538 optical tweezer experiments have found that kinesin detachment rates increase exponentially with force
539 (58,59,66), recent theoretical and experimental work has suggested that forces perpendicular to the
540 microtubule inherent to the geometry of these experiments may be contributing to the detachment rate.
541 In support of this, experiments using a three-bead assay that almost fully eliminate these vertical forces
542 found that the kinesin-1 detachment rate was approximately independent of load (58). Incorporating this
543 'ideal-bond' for kinesin into our model strongly diminished the minus-end side peak in the velocity
544 distribution; thus, our simulations support the hypothesis that against forces oriented purely parallel to
545 the microtubule, the kinesin detachment is independent of load. We also examined a catch-bond model

546 for kinesin, and found a further increase in the amplitude of the central velocity peak with increasing catch
547 bond properties (Fig. S5). Thus, our results are consistent with possibility that kinesin has catch-bond
548 behavior under some circumstances, but an idea-bond for kinesin was sufficient in our simulations to
549 match the experimental data.

550 We also found that incorporating a load-independent detachment rate for DDB diminished the fast plus-
551 end velocities seen in the simulations, better matching the experimental data. This result can be
552 understood simply as DDB remaining bound to the microtubule against the pulling forces of kinesin, thus
553 preventing durations in which DDB is detached and kinesin is moving at its unloaded speed. A DDB ideal-
554 bond model is supported by experiments with activator-free dynein and with isolated vesicles, which
555 found evidence that dynein has catch-bond behavior under some conditions (29,57), though we note that
556 a DDB optical trapping study by Elshenawy et al. found an exponential dependence of DDB detachment
557 with load (33). However, it remains a possibility that, as has been shown for kinesin-1 (30,33,59), vertical
558 forces inherent to the single-bead optical trapping assay may contribute to detachment of DDB. Thus, our
559 simulations put forth the testable hypothesis that when pulling exclusively against hindering loads
560 oriented parallel to the microtubule, DDB detachment is independent of load over the forces generated
561 by a single kinesin motor. As with kinesin, our results were also consistent with DDB catch bond behavior
562 (Fig. S3A), but an ideal bond was sufficient to match the simulations to the experiments.

563 Incorporating a fast kinesin-1 reattachment rate was another important modification that helped to bring
564 the simulations into alignment with the experimental data. In particular, the fast kinesin-1 reattachment
565 rate diminished the minus-end velocity side peak, which can be understood as minimizing the time that
566 DDB moves at its unloaded velocity. Our basic model used a $k_{reattach}$ value of 5 s^{-1}, which was initially
567 determined in a study that measured motor-driven deformations of giant unilamellar vesicles (53), was
568 later supported by experiments that used DNA to connect two kinesins (48), and which has been
569 employed in a number of modeling studies (e.g. (28)). However, three recent optical tweezer studies
570 found that against hindering loads, kinesin-1 can slip backward in multiple 8 nm intervals and rapidly
571 reengage with the microtubule at rates consistent with our 50 s^{-1} reattachment rate (58,67,68). These
572 experiments suggest that against a hindering loads oriented parallel to the microtubule, kinesin-1 enters
573 a weak-binding state in which it slips backward, and then rapidly reestablishes a strong-binding state. We
574 also note that this 50 s^{-1} reattachment rate is still below the 125 s^{-1} reattachment rate predicted from
575 multiplying the bimolecular on-rate of kinesin in solution by the effective tubulin concentration when two
576 motors are connected through a DNA linker (48). Thus, our simulations put forth the testable hypothesis

577 that when pulling against hindering loads oriented parallel to the microtubule, the kinesin-1 reattachment
578 rate is 50 s^{-1} or faster. A possible mechanism to explain this phenomenon is that if a kinesin slips or
579 detaches against a load oriented parallel to the microtubule, the motor is presented with multiple sites of
580 reattachment as it slides backward. Further, it is possible that if the motor reattaches against a hindering
581 load, the force enhances the rate of ADP release, which maximizes the probability that the motor enters
582 a strongly-bound state and restarts its walking cycle.

583 The model adjustment that most influenced the position of the central peak in the instantaneous velocity
584 distribution was altering the relative stall forces of DDB and kinesin-1, highlighting that the antagonistic
585 motors rapidly establish a "draw" where each is pulling at near its maximum force. The paired
586 modification of reducing the kinesin-1 stall force from 8 pN down to 6 pN and increasing the DDB stall
587 force from 3.6 pN up to 6 pN shifted the central peak leftward by roughly ~140 nm/s to match the
588 experimental peak (Fig. 6B). A large body of experiments support a kinesin-1 stall force in the range of 6
589 pN (29,46,60-64), justifying this modification. For DDB, one justification for increasing the stall force is
590 that the lower value we started with was taken from a study using single-bead tweezer geometry (33),
591 and it is possible that in the geometry of these DDB-kinesin pairs where forces are oriented solely parallel
592 to the microtubule, the DDB stall forces are closer to the ~6 pN of kinesin-1 (Fig. 3D). Related to the stall
593 force, we also found that slowing the DDB backstepping rate shifted the central velocity peak leftward.
594 This shift makes sense in cases where the kinesin stall force is greater than the DDB stall force, meaning
595 that DDB is under superstall forces and stepping backward at 15 s^{-1} (Fig. 5C and S3C). However, we note
596 that when stall forces were matched, the DDB backstepping rate did not have a strong effect on the
597 velocity distribution (Fig. S6). Hence, although single-bead optical tweezer experiments measured a DDB
598 backstepping rate of 15 s^{-1} (33), our simulations put forward the testable hypothesis that the DDB
599 backstepping rate may be smaller in the absence of any vertical forces.

600 Another model adjustment that had a surprising effect was increasing the stiffness of the linkages
601 connecting the two motors to the cargo. When model and experiments were compared by analyzing
602 instantaneous velocities, a 'recoil' effect becomes apparent following detachment of one of the motors
603 (usually kinesin in our simulations). Thus, the simulations provide a lower limit of 0.2 pN/nm for the motor
604 stiffness and make the testable prediction that if a more compliant DNA linkage were used to connect the
605 motors, the instantaneous velocity distribution would reveal apparent fast velocities due to large
606 displacement recoil events. Additionally, a more compliant linkage between the motors would be relevant

607 to the transport of large (0.1 – 1 micron) vesicles in cells, where motor forces are sufficient to deform the
608 membrane.

609 Despite the large body of single-molecule data describing their motor properties, it remains challenging
610 to predict the bidirectional dynamics that will result from antagonistic kinesin and dynein motor pairs. In
611 the present work we find that by using experimental data to constrain model simulations, mechanistic
612 insights can be generated into how kinesin and DDB operate in antagonistic pairs. Our simulations support
613 a model (Fig. 6D) in which: 1) Over the range of forces generated by the motors, the detachment rate of
614 both kinesin-1 and DDB is insensitive to load; 2) In the two-motor geometry examined, the kinesin-1 and
615 DDB stall forces are similar; 3) kinesin-1 reattaches to the microtubule at 50 s^{-1} in the geometry of these
616 motor pairs; and 4) when modeled as linear springs, motor stiffness is at least 0.2 pN/nm. These model-
617 generated hypotheses generate testable predictions for future single-molecule experiments. Furthermore,
618 by identifying motor parameters that are the strongest determinants of bidirectional transport, this work
619 provides a framework to interpret how diverse kinesins, different activating dynein adapters, and motor-
620 cargo stiffness will affect the resulting bidirectional transport of intracellular cargo.

621

Author Contributions

T-C.M. and W.O.H. designed research, T-C.M. performed all simulations and carried out analysis, Q.F. and A.M.G. carried out experiments and experimental data analysis. T-C.M., W.O.H. and A.M.G. wrote the manuscript, and all authors edited the manuscript.

Declaration of Interests

The authors declare no competing interests.

Acknowledgements

The authors thank George Ohashi and John Fricks who helped formulate a previous iteration of the current model, as well as members of the Hancock lab who provided helpful input. We thank an anonymous reviewer for suggesting an objective parameter optimization strategy. This work was supported by NIH grants R01GM076476, 1R01GM122082 and R35GM139568 to W.O.H., and F32GM137487 to A.M.G.

637 **References**:

638 1. Encalada, S. E., L. Szpankowski, C. H. Xia, and L. S. B. Goldstein. 2011. Stable Kinesin and Dynein
639 Assemblies Drive the Axonal Transport of Mammalian Prion Protein Vesicles. *Cell*. 144(4):551-
640 565, doi: 10.1016/j.cell.2011.01.021.
641 2. Leidel, C., R. A. Longoria, F. M. Gutierrez, and G. T. Shubeita. 2012. Measuring Molecular Motor
642 Forces In Vivo: Implications for Tug-of-War Models of Bidirectional Transport. *Biophysical*
643 *Journal*. 103(3):492-500, doi: 10.1016/j.bpj.2012.06.038.
644 3. Ligon, L. A., M. Tokito, J. M. Finklestein, F. E. Grossman, and E. L. F. Holzbaur. 2004. A Direct
645 Interaction between Cytoplasmic Dynein and Kinesin I May Coordinate Motor Activity. *Journal of*
646 *Biological Chemistry*. 279(18):19201-19208, doi: 10.1074/jbc.m313472200.
647 4. Mizuno, N., S. Toba, M. Edamatsu, J. Watai-Nishii, N. Hirokawa, Y. Y. Toyoshima, and M.
648 Kikkawa. 2004. Dynein and kinesin share an overlapping microtubule-binding site. *The EMBO*
649 *Journal*. 23(13):2459-2467, doi: 10.1038/sj.emboj.7600240.
650 5. Gross, S. P., M. A. Welte, S. M. Block, and E. F. Wieschaus. 2000. Dynein-mediated cargo
651 transport in vivo: A switch controls travel distance. *J Cell Biol*. 148(5):945-955, doi:
652 10.1083/jcb.148.5.945.
653 6. Hendricks, A. G., E. Perlson, J. L. Ross, H. W. Schroeder, M. Tokito, and E. L. F. Holzbaur. 2010.
654 Motor Coordination via a Tug-of-War Mechanism Drives Bidirectional Vesicle Transport. *Current*
655 *Biology*. 20(8):697-702, doi: 10.1016/j.cub.2010.02.058.
656 7. Holzbaur, E. L., and Y. E. Goldman. 2010. Coordination of molecular motors: from in vitro assays
657 to intracellular dynamics. *Current Opinion in Cell Biology*. 22(1):4-13, doi:
658 10.1016/j.ceb.2009.12.014.
659 8. Encalada, S. E., and L. S. B. Goldstein. 2014. Biophysical Challenges to Axonal Transport: Motor-
660 Cargo Deficiencies and Neurodegeneration. *Annual Review of Biophysics*. 43(1):141-169, doi:
661 10.1146/annurev-biophys-051013-022746.
662 9. Hancock, W. O. 2014. Bidirectional cargo transport: moving beyond tug of war. *Nature Reviews*
663 *Molecular Cell Biology*. 15(9):615-628, doi: 10.1038/nrm3853.
664 10. Goldstein, L. S. B. 2001. Kinesin molecular motors: Transport pathways, receptors, and human
665 disease. *J Gen Physiol*. 118(1):4a-4a.
666 11. Eschbach, J., and L. Dupuis. 2011. Cytoplasmic dynein in neurodegeneration. *Pharmacol*
667 *Therapeut*. 130(3):348-363, doi: 10.1016/j.pharmthera.2011.03.004.
668 12. Cai, D. W., K. J. Verhey, and E. Meyhofer. 2007. Tracking single kinesin molecules in the
669 cytoplasm of mammalian cells. *Biophysical Journal*. 92(12):4137-4144, doi:
670 10.1529/biophysj.106.100206.
671 13. Courty, S., C. Luccardini, Y. Bellaiche, G. Cappello, and M. Dahan. 2006. Tracking individual
672 kinesin motors in living cells using single quantum-dot imaging. *Nano Lett*. 6(7):1491-1495, doi:
673 10.1021/nl060921t.
674 14. Fridman, V., A. Gerson-Gurwitz, O. Shapira, N. Movshovich, S. Lakamper, C. F. Schmidt, and L.
675 Gheber. 2013. Kinesin-5 Kip1 is a bi-directional motor that stabilizes microtubules and tracks
676 their plus-ends in vivo. *Journal of Cell Science*. 126(18):4147-4159, doi: 10.1242/jcs.125153.
677 15. Ma, S., and R. L. Chisholm. 2002. Cytoplasmic dynein-associated structures move bidirectionally
678 in vivo. *Journal of Cell Science*. 115(7):1453-1460.
679 16. Reck-Peterson, S. L., A. Yildiz, A. P. Carter, A. Gennerich, N. Zhang, and R. D. Vale. 2006. Single-
680 Molecule Analysis of Dynein Processivity and Stepping Behavior. *Cell*. 126(2):335-348, doi:
681 10.1016/j.cell.2006.05.046.
682 17. Schnitzer, M. J., K. Visscher, and S. M. Block. 2000. Force production by single kinesin motors.
683 *Nature Cell Biology*. 2(10):718-723, doi: 10.1038/35036345.

18. Visscher, K., M. J. Schnitzer, and S. M. Block. 1999. Single kinesin molecules studied with a molecular force clamp. *Nature*. 400(6740):184-189, doi: 10.1038/22146.
19. D'Souza, A. I., R. Grover, G. A. Monzon, L. Santen, and S. Diez (2022). Vesicles driven by dynein and kinesin exhibit directional reversals without external regulators. doi: 10.1101/2022.09.27.509758 (preprint posted September 28, 2022).
20. Monzon, G. A., L. Scharrel, A. Dsouza, V. Henrichs, L. Santen, and S. Diez. 2020. Stable tug-of-war between kinesin-1 and cytoplasmic dynein upon different ATP and roadblock concentrations. *Journal of Cell Science*. 133(22):jcs249938, doi: 10.1242/jcs.249938.
21. Hu, J., and N. D. Derr. 2019. Production of Dynein and Kinesin Motor Ensembles on DNA Origami Nanostructures for Single Molecule Observation. *Journal of Visualized Experiments*.(152), doi: 10.3791/60369.
22. Arpağ, G., S. R. Norris, S. I. Mousavi, V. Soppina, K. J. Verhey, W. O. Hancock, and E. Tüzel. 2019. Motor Dynamics Underlying Cargo Transport by Pairs of Kinesin-1 and Kinesin-3 Motors. *Biophysical Journal*. 116(6):1115-1126, doi: 10.1016/j.bpj.2019.01.036.
23. Gicking, A. M., T. C. Ma, Q. Z. Feng, R. Jiang, S. Badieyan, M. A. Cianfrocco, and W. O. Hancock. 2022. Kinesin-1,-2, and-3 motors use family-specific mechanochemical strategies to effectively compete with dynein during bidirectional transport. *Elife*. 11, doi: 10.7554/eLife.82228.
24. Dallon, J. C., C. Leduc, S. Etienne-Manneville, and S. Portet. 2019. Stochastic modeling reveals how motor protein and filament properties affect intermediate filament transport. *Journal of Theoretical Biology*. 464:132-148, doi: 10.1016/j.jtbi.2018.12.022.
25. Altaner, B., A. Wachtel, and J. Vollmer. 2015. Fluctuating currents in stochastic thermodynamics. II. Energy conversion and nonequilibrium response in kinesin models. *Phys Rev E*. 92(4), doi: 10.1103/PhysRevE.92.042133.
26. Puri, P., N. Gupta, S. Chandel, S. Naskar, A. Nair, A. Chaudhuri, M. K. Mitra, and S. Muhuri. 2019. Dynein catch bond as a mediator of codependent bidirectional cellular transport. *Physical Review Research*. 1(2), doi: 10.1103/physrevresearch.1.023019.
27. Ohashi, K. G., L. Han, B. Mentley, J. Wang, J. Fricks, and W. O. Hancock. 2019. Load-dependent detachment kinetics plays a key role in bidirectional cargo transport by kinesin and dynein. *Traffic*. 20(4):284-294, doi: 10.1111/tra.12639.
28. Muller, M. J. I., S. Klumpp, and R. Lipowsky. 2008. Tug-of-war as a cooperative mechanism for bidirectional cargo transport by molecular motors. *P Natl Acad Sci USA*. 105(12):4609-4614, doi: 10.1073/pnas.0706825105.
29. Kunwar, A., S. K. Tripathy, J. Xu, M. K. Mattson, P. Anand, R. Sigua, M. Vershinin, R. J. McKenney, C. C. Yu, A. Mogilner, and S. P. Gross. 2011. Mechanical stochastic tug-of-war models cannot explain bidirectional lipid-droplet transport. *P Natl Acad Sci USA*. 108(47):18960-18965, doi: 10.1073/pnas.1107841108.
30. Howard, J., and W. O. Hancock. 2020. Three Beads Are Better Than One. *Biophysical Journal*. 118(1):1-3, doi: 10.1016/j.bpj.2019.12.001.
31. Pyrpassopoulos, S., H. Shuman, and E. M. Ostap. 2020. Modulation of Kinesin's Load-Bearing Capacity by Force Geometry and the Microtubule Track. *Biophysical Journal*. 118(1):243-253, doi: 10.1016/j.bpj.2019.10.045.
32. Belyy, V., M. A. Schlager, H. Foster, A. E. Reimer, A. P. Carter, and A. Yildiz. 2016. The mammalian dynein–dynactin complex is a strong opponent to kinesin in a tug-of-war competition. *Nature Cell Biology*. 18(9):1018-1024, doi: 10.1038/ncb3393.
33. Elshenawy, M. M., J. T. Canty, L. Oster, L. S. Ferro, Z. Zhou, S. C. Blanchard, and A. Yildiz. 2019. Cargo adaptors regulate stepping and force generation of mammalian dynein–dynactin. *Nature Chemical Biology*. 15(11):1093-1101, doi: 10.1038/s41589-019-0352-0.

731 34. Feng, Q., A. M. Gicking, and W. O. Hancock. 2020. Dynactin p150 promotes processive motility
732 of DDB complexes by minimizing diffusional behavior of dynein. *Molecular Biology of the Cell*.
733 31(8):782-792, doi: 10.1091/mbc.e19-09-0495.
734 35. Gutierrez, P. A., B. E. Ackermann, M. Vershinin, and R. J. McKenney. 2017. Differential effects of
735 the dynein-regulatory factor Lissencephaly-1 on processive dynein-dynactin motility. *Journal of*
736 *Biological Chemistry*. 292(29):12245-12255, doi: 10.1074/jbc.m117.790048.
737 36. King, S. J., and T. A. Schroer. 2000. Dynactin increases the processivity of the cytoplasmic dynein
738 motor. *Nature Cell Biology*. 2(1):20-24, doi: 10.1038/71338.
739 37. McKenney, R. J., W. Huynh, M. E. Tanenbaum, G. Bhabha, and R. D. Vale. 2014. Activation of
740 cytoplasmic dynein motility by dynactin-cargo adapter complexes. *Science*. 345(6194):337-341,
741 doi: 10.1126/science.1254198.
742 38. Ross, J. L., K. Wallace, H. Shuman, Y. E. Goldman, and E. L. F. Holzbaur. 2006. Processive
743 bidirectional motion of dynein-dynactin complexes in vitro. *Nature Cell Biology*. 8(6):562-570,
744 doi: 10.1038/ncb1421.
745 39. Sanghavi, P., P. Kumar, A. Roy, M. S. Madhusudhan, and R. Mallik. 2021. On and off controls
746 within dynein-dynactin on native cargoes. *P Natl Acad Sci USA*. 118(23), doi:
747 10.1073/pnas.2103383118.
748 40. Schlager, M. A., H. T. Hoang, L. Urnavicius, S. L. Bullock, and A. P. Carter. 2014. In vitro
749 reconstitution of a highly processive recombinant human dynein complex. *The EMBO Journal*.
750 33(17):1855-1868, doi: 10.15252/embj.201488792.
751 41. Gillespie, D. T. 1977. Exact Stochastic Simulation of Coupled Chemical-Reactions. *J Phys Chem-*
752 *Us*. 81(25):2340-2361, doi: 10.1021/j100540a008.
753 42. Coppin, C. M., D. W. Pierce, L. Hsu, and R. D. Vale. 1997. The load dependence of kinesin's
754 mechanical cycle. *Proceedings of the National Academy of Sciences*. 94(16):8539-8544, doi:
755 10.1073/pnas.94.16.8539.
756 43. Bruno, L., M. Salierno, D. E. Wetzler, M. A. Despósito, and V. Levi. 2011. Mechanical Properties
757 of Organelles Driven by Microtubule-Dependent Molecular Motors in Living Cells. *PLoS ONE*.
758 6(4):e18332, doi: 10.1371/journal.pone.0018332.
759 44. Oiwa, K., and H. Sakakibara. 2005. Recent progress in dynein structure and mechanism. *Curr*
760 *Opin Cell Biol*. 17(1):98-103, doi: 10.1016/j.ceb.2004.12.006.
761 45. Howard, J. 2001. Mechanics of motor proteins and the cytoskeleton. Sinauer Associates,
762 Publishers, Sunderland, Mass.
763 46. Andreasson, J. O. L., S. Shastry, W. O. Hancock, and S. M. Block. 2015. The Mechanochemical
764 Cycle of Mammalian Kinesin-2 KIF3A/B under Load. *Current Biology*. 25(9):1166-1175, doi:
765 10.1016/j.cub.2015.03.013.
766 47. Andreasson, J. O., B. Milic, G.-Y. Chen, N. R. Guydosh, W. O. Hancock, and S. M. Block. 2015.
767 Examining kinesin processivity within a general gating framework. *eLife*. 4, doi:
768 10.7554/elife.07403.
769 48. Feng, Q., K. J. Mickolajczyk, G. Y. Chen, and W. O. Hancock. 2018. Motor Reattachment Kinetics
770 Play a Dominant Role in Multimotor-Driven Cargo Transport. *Biophys J*. 114(2):400-409, doi:
771 10.1016/j.bpj.2017.11.016.
772 49. Urnavicius, L., K. Zhang, A. G. Diamant, C. Motz, M. A. Schlager, M. M. Yu, N. A. Patel, C. V.
773 Robinson, and A. P. Carter. 2015. The structure of the dynactin complex and its interaction with
774 dynein. *Science*. 347(6229):1441-1446, doi: 10.1126/science.aaa4080.
775 50. Kaan, H. Y. K., D. D. Hackney, and F. Kozielski. 2011. The Structure of the Kinesin-1 Motor-Tail
776 Complex Reveals the Mechanism of Autoinhibition. *Science*. 333(6044):883-885, doi:
777 10.1126/science.1204824.

51. Carter, A. P., C. Cho, L. Jin, and R. D. Vale. 2011. Crystal Structure of the Dynein Motor Domain. *Science*. 331(6021):1159-1165, doi: 10.1126/science.1202393.
52. Beeg, J., S. Klumpp, R. Dimova, R. S. Gracia, E. Unger, and R. Lipowsky. 2008. Transport of beads by several kinesin motors. *Biophysical Journal*. 94(2):532-541, doi: 10.1529/biophysj.106.097881.
53. Leduc, C., O. Campas, K. B. Zeldovich, A. Roux, P. Jolimaitre, L. Bourel-Bonnet, B. Goud, J. F. Joanny, P. Bassereau, and J. Prost. 2004. Cooperative extraction of membrane nanotubes by molecular motors. *P Natl Acad Sci USA*. 101(49):17096-17101, doi: 10.1073/pnas.0406598101.
54. Johnson, C. M. F. J. D. B., Anthony; Jung, P 2020. Dynamic catch-bonding generates the large stall forces of cytoplasmic dynein. *Physical Biology*. 17, doi: 10.1088/1478-3975/ab907.
55. Nair, A., S. Chandel, M. K. Mitra, S. Muhuri, and A. Chaudhuri. 2016. Effect of catch bonding on transport of cellular cargo by dynein motors. *Phys Rev E*. 94(3), doi: 10.1103/PhysRevE.94.032403.
56. Thomas, W. E., V. Vogel, and E. Sokurenko. 2008. Biophysics of catch bonds. *Annual Review of Biophysics*. 37:399-416, doi: 10.1146/annurev.biophys.37.032807.125804.
57. Rai, A. K., A. Rai, A. J. Ramaiya, R. Jha, and R. Mallik. 2013. Molecular Adaptations Allow Dynein to Generate Large Collective Forces inside Cells. *Cell*. 152(1-2):172-182, doi: 10.1016/j.cell.2012.11.044.
58. Pyrpassopoulos, S., A. M. Gicking, T. M. Zaniewski, W. O. Hancock, and E. M. Ostap. 2023. KIF1A is kinetically tuned to be a superengaging motor under hindering loads. *Proceedings of the National Academy of Sciences*. 120(2), doi: 10.1073/pnas.2216903120.
59. Khataee, H., and J. Howard. 2019. Force Generated by Two Kinesin Motors Depends on the Load Direction and Intermolecular Coupling. *Phys Rev Lett*. 122(18), doi: 10.1103/PhysRevLett.122.188101.
60. Svoboda, K., and S. M. Block. 1994. Force and Velocity Measured for Single Kinesin Molecules. *Cell*. 77(5):773-784, doi: 10.1016/0092-8674(94)90060-4.
61. Kawaguchi, K., and S. Ishiwata. 2000. Temperature dependence of force, velocity, and processivity of single kinesin molecules. *Biochem Bioph Res Co*. 272(3):895-899, doi: 10.1006/bbrc.2000.2856.
62. Gittes, F., E. Meyhofer, S. Baek, and J. Howard. 1996. Directional loading of the kinesin motor molecule as it buckles a microtubule. *Biophysical Journal*. 70(1):418-429, doi: 10.1016/S0006-3495(96)79585-1.
63. Hunt, A. J., F. Gittes, and J. Howard. 1994. The Force Exerted by a Single Kinesin Molecule against a Viscous Load. *Biophysical Journal*. 67(2):766-781, doi: 10.1016/S0006-3495(94)80537-5.
64. Budaitis, B. G., S. Jariwala, L. Rao, Y. Yue, D. Sept, K. J. Verhey, and A. Gennerich. 2021. Pathogenic mutations in the kinesin-3 motor KIF1A diminish force generation and movement through allosteric mechanisms. *J Cell Biol*. 220(4), doi: 10.1083/jcb.202004227.
65. Derr, N. D., B. S. Goodman, R. Jungmann, A. E. Leschziner, W. M. Shih, and S. L. Reck-Peterson. 2012. Tug-of-War in Motor Protein Ensembles Revealed with a Programmable DNA Origami Scaffold. *Science*. 338(6107):662-665, doi: 10.1126/science.1226734.
66. Guo, S. K., X. X. Shi, P. Y. Wang, and P. Xie. 2019. Force dependence of unbinding rate of kinesin motor during its processive movement on microtubule. *Biophys Chem*. 253:106216, doi: 10.1016/j.bpc.2019.106216.
67. Sudhakar, S., M. K. Abdosamadi, T. J. Jachowski, M. Bugiel, A. Jannasch, and E. Schaffer. 2021. Germanium nanospheres for ultraresolution picotensiometry of kinesin motors. *Science*. 371(6530):692-+, doi: 10.1126/science.abd9944.

68. Toleikis, A., N. J. Carter, and R. A. Cross. 2020. Backstepping Mechanism of Kinesin-1. *Biophysical Journal*. 119(10):1984-1994, doi: 10.1016/j.bpj.2020.09.034.

Supplemental Figures and Tables:

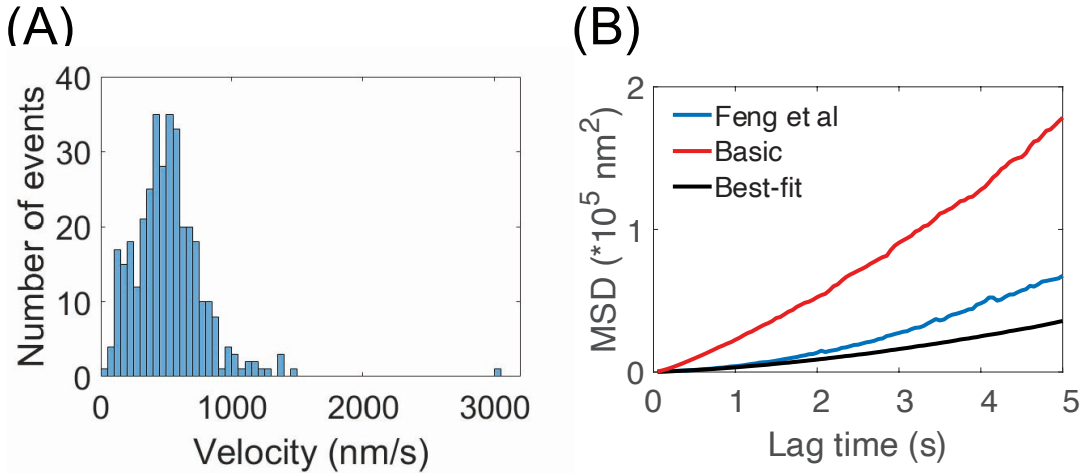

Figure S1. (A) Distribution of trace velocities of isolated kinesin-1 in the dynein motility buffer used in Kin-DDB experiments (1). Dynein motility buffer consists of 30 mM HEPES, 50 mM potassium acetate, 2 mM magnesium acetate, 1 mM EGTA and 10% glycerol, supplemented with 2 mg/ml casein, 20 mM glucose, 37 mM βME, glucose oxidase, catalase, 10 mM Taxol, and 2 mM ATP. The mean velocity of 515 nm/s was used for the unloaded kinesin-1 velocity in the simulations. (B) Mean squared displacement (MSD) analysis of experimental data from Feng et al. (1) and Basic and Best-fit model results from this study. Curves were fit with the equation: $MSD = V^2t^2 + 2Dt$, where V is velocity, D is the apparent diffusion coefficient, and t is the lag time. Fit results are $V = 49\ nm/s, D = 996\ nm^2/s$ for experimental data, $V = 49nm/s, D = 11{,}800\ nm^2/s$ from the basic model, and $V = 32\ nm/s, D = 1812\ nm^2/s$ from the best-fit model.

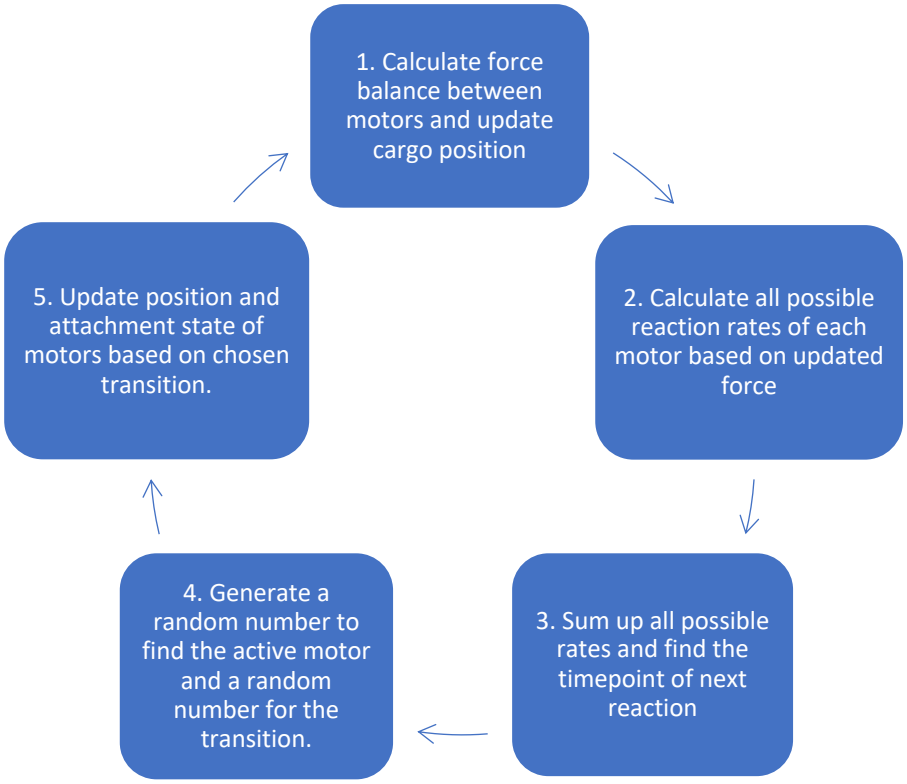

Figure S2. Flow chart for stochastic bidirectional stepping algorithm. The initial positions of both motors and the cargo are at the origin. The first step is to update the force balance between the motors and use this do define the cargo position. The second step is to calculate all possible reaction rates based on the forces applied to each motor. The third step is to use a random number to find the timepoint when the next reaction occurs based on Eq. (2) in Methods. The fourth step is to use one random number to choose which motor is active and a second random number to choose which transition the active motor will make. Finally, the motor position and attachment states are updated. The steps are repeated until both motors detach from the microtubule or until the maximum simulation time is achieved.

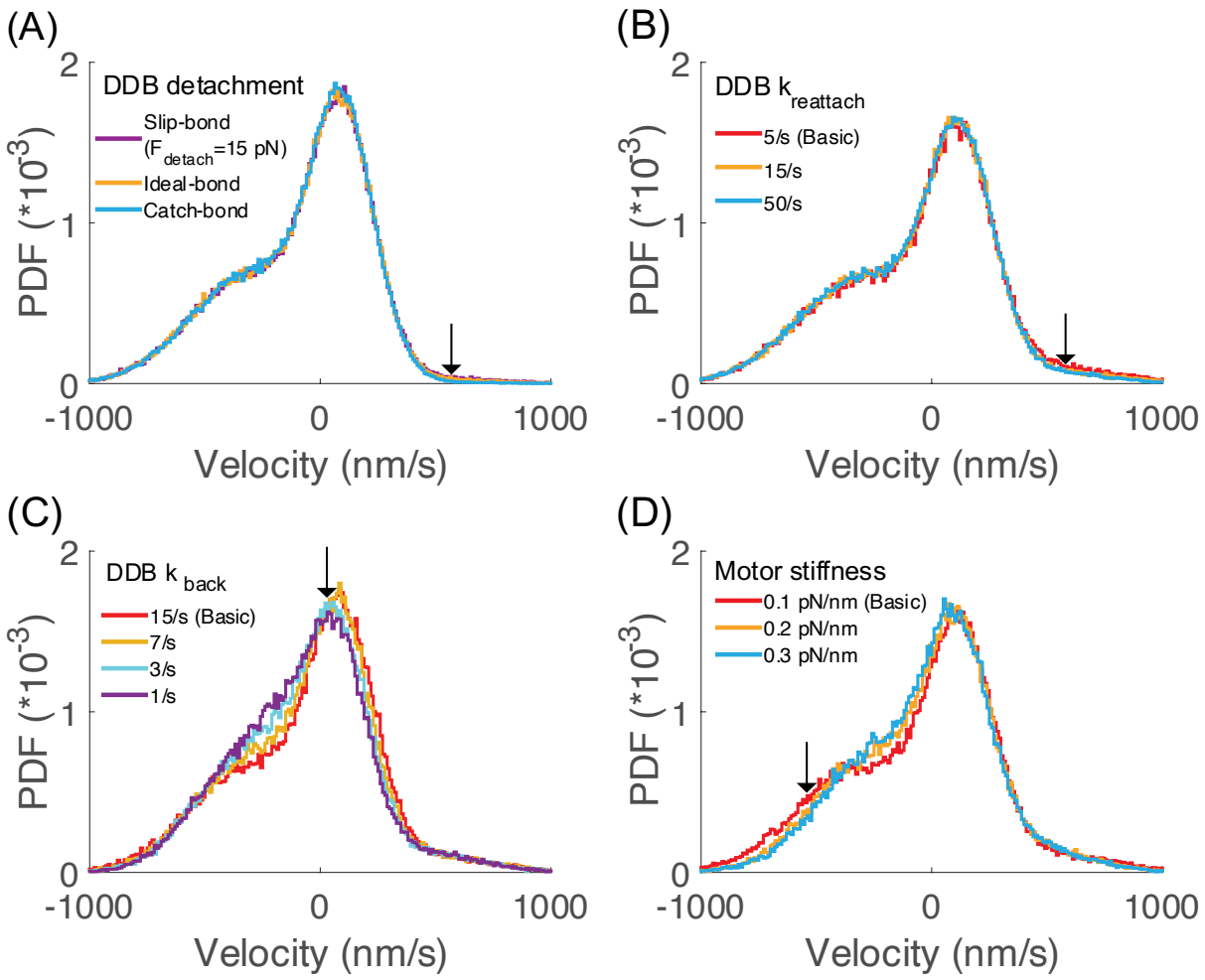

Figure S3. Effect of changing DDB mechanochemical properties and motor stiffnesses on the instantaneous velocity distribution in the 'basic' model. (A) Comparison between different load-dependencies of the DDB detachment rate. The slip-bond with F_{detach} = 15 pN was taken from Fig. 3C, an ideal-bond corresponds to F_{detach} set to infinity, and the catch-bond used F_{detach} = -3 pN such that detachment slows with increasing force. (B) Effect of altering the DDB reattachment rate, showing only a very small effect on the plus-end side peak. (C) Effect of altering the DDB backstepping rate, k_{back}, showing a small leftward shift of the central velocity peak with slower backstepping. (D) Effect of increasing the motor stiffness was to reduce the minus-end velocity peak.

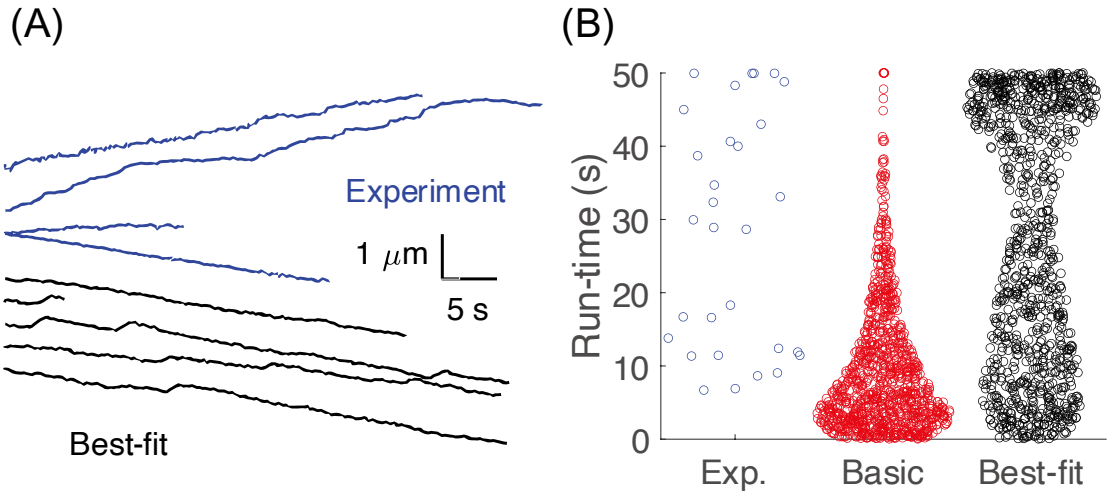

Figure S4. (A) Example 50-second traces from tracking experiment (1) and simulations of the best-fit model. (B) Distribution of run durations from experimental data (blue), basic model (red) and best-fit model (black). The best-fit model had longer run durations that more closely matched the experimental data. Maximum duration of 50 s was set by movie duration from experiments.

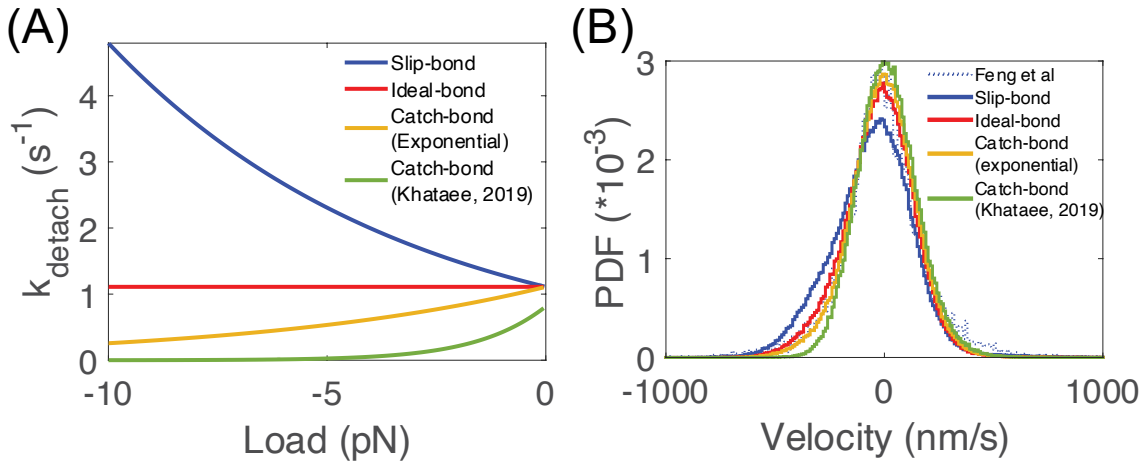

Figure S5. (A) Different models of kinesin detachment under horizontal hindering loads. The slip-bond model (blue) is based on experimental data from Andreasson et al. (2). The ideal-bond model (red) used a load-independent detachment rate, $k_{detach}(F) = k^0_{detach}$, where k^0_{detach} is unloaded detachment rate. The exponential catch-bond model (yellow curve) reversed the sign of the F_{detach}= 6.8 pN used for the slip bond, such that $k_{detach}(F) = k^0_{detach} * e^{\frac{-|F|}{F_{detach}}}$. The alternate catch-bond model (green) is the detachment rate under horizontal load calculated by Khataee et al. (3). (B) The instantaneous velocity distribution of 'best-fit' kin-DDB model with different kinesin detachment models applied.

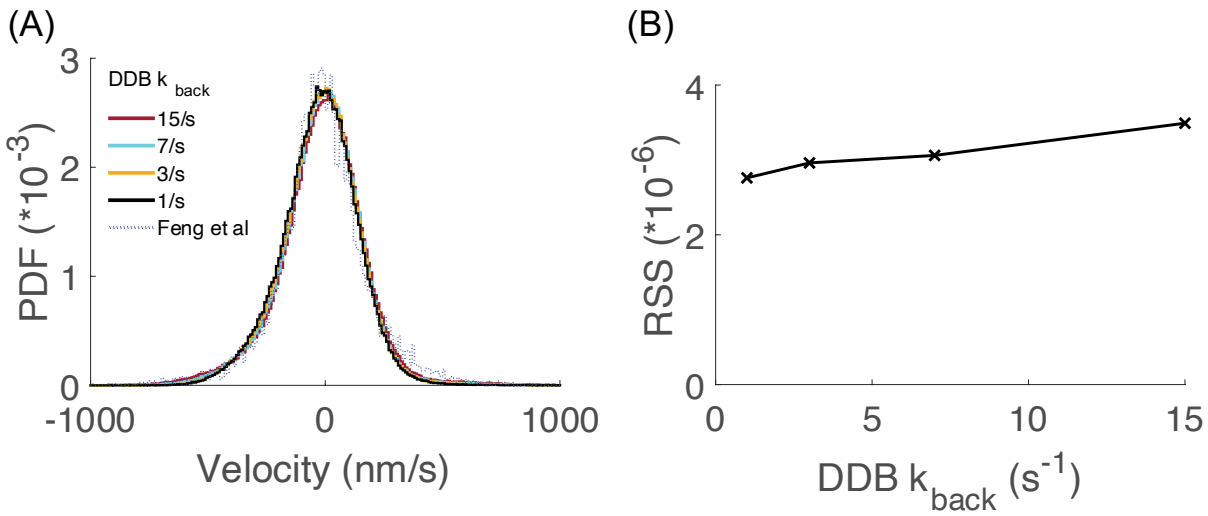

Figure S6. Effect of changing the DDB backstepping rate in the 'best-fit' model. (A) Instantaneous velocity distribution, showing the small effect of changing the DDB backstepping rate. (B) Residual sum of squares between simulation and experiment for 'best-fit' model with different DDB backstepping rates.

	Kinesin-1	DDB
Forward stepping rate under assisting load	$k^0_{forward}$	$v(F) = v_{min} * \left[1 - e^{(F_{stall}-F)*\frac{d}{k_B T}}\right]$ $k_{forward}(F) = \frac{v(F)}{8\,nm} + k_{back}$
Forward stepping rate under hindering load	$k_{forward}(F) = \left(k_{back} - k^0_{forward}\right) * \left(\frac{\lvert F\rvert}{F_{stall}}\right) + k^0_{forward}$	
Forward stepping rate when rate is negative	0 s^{-1}	
Backward stepping rate	Load independent	
Detachment rate	$k_{detach}(F) = k^0_{detach} * e^{\frac{\lvert F\rvert}{F_{detach}}}$	
Reattachment rate	Load independent	

Table S1. The models for load-dependent motor mechanisms used in stochastic stepping model.

Parameter	Better-fit model	
	Kinesin-1	**DDB**
Unloaded velocity (nm/s)	515	328
Backstepping rate (s^{-1})	3	15
Stall force (pN)	6[b]	3.6
Unloaded detachment rate (s^{-1})[a]	1.11	0.1
Detachment force (pN)	Ideal	Ideal
Reattachment rate (s^{-1})	50[b]	5
Stiffness (pN/nm)	0.1068	0.1068
Residual sum of squares (RSS)	$4.29*10^{-5}$	

Table S2. Parameters used for the 'better-fit' model.

[a] For kinesin under assisting loads, the unloaded detachment rate extrapolation was 7.4 s^{-1} and detachment force was 12.8 pN based on (2). For DDB under assisting loads, the unloaded detachment rate and detachment force were identical to the hindering load condition. Ideal bond (load-independent detachment) corresponds to F_{detach} equal to infinity.

[b] The parameters used in "better-fit" were established by results of parameter sensitivity tests in simulation.

Reference:

1. Feng, Q., A. M. Gicking, and W. O. Hancock. 2020. Dynactin p150 promotes processive motility of DDB complexes by minimizing diffusional behavior of dynein. *Molecular Biology of the Cell*. 31(8):782-792, doi: 10.1091/mbc.e19-09-0495.
2. Andreasson, J. O., B. Milic, G.-Y. Chen, N. R. Guydosh, W. O. Hancock, and S. M. Block. 2015. Examining kinesin processivity within a general gating framework. *eLife*. 4, doi: 10.7554/elife.07403.
3. Khataee, H., and J. Howard. 2019. Force Generated by Two Kinesin Motors Depends on the Load Direction and Intermolecular Coupling. *Phys Rev Lett*. 122(18), doi: 10.1103/PhysRevLett.122.188101.